Contractile homeostasis is an intrinsic barrier to cardiac regeneration

Authors: Kang-Wei Wang[1,2], Gang Xie[1,2], Xin-Hui Lai[1,2], Yi-Xia Wu[1,2], Shuang-Jin Ding[1,2], Yuhan Zhang[3], Huiqing Cao[1,2*] and Yangming Wang[1,2,4*]

Affiliations:

1 State Key Laboratory of Gene Function and Modulation Research, Institute of Molecular Medicine, College of Future Technology, Peking University, Beijing, 100871, China

2 Beijing Advanced Center of RNA Biology (BEACON), Peking University, Beijing, 100871, China

3 Faculty of Medicine, Dentistry and Health Sciences (MDHS), The University of Melbourne, Melbourne, Victoria3010, Australia

4 Southwest United Graduate School, Kunming, 650092, China

*To whom correspondence should be addressed: Dr. Huiqing Cao, Email: caohuiqing@pku.edu.cn; and Dr. Yangming Wang, Email: yangming.wang@pku.edu.cn

Abstract

Adult mammalian cardiomyocytes (CMs) acquire powerful contractile function as they mature, yet lose regenerative competence. Whether this functional transition actively imposes regenerative arrest is unknown. Here we show that the postnatally induced transcription factor KLF3 establishes contractile homeostasis as an intrinsic barrier to CM regenerative competence. CM-specific *Klf3* deletion enhances Ca^{2+} cycling and contraction, reactivates CM cell-cycle activity and improves cardiac repair after myocardial infarction (MI). Integrated transcriptomic, CUT&Tag and lipidomic analyses reveal that KLF3 represses contractile and Ca^{2+}-handling genes and limits glycosphingolipid biosynthesis. Disruption of contractile homeostasis, by either *Klf3* deficiency or pharmacological contractile stimulation, increases membrane mechanical stress and activates neutral sphingomyelinase (nSMase)-dependent sphingolipid remodeling; conversely, nSMase inhibition abolishes the proliferative response. Lactosylceramide (LacCer), a major sphingolipid metabolite elevated in *Klf3*-deficient hearts, is sufficient to stimulate CM cell-cycle re-entry and promote post-infarction repair. These findings identify contractile homeostasis as an active maturation-linked brake on mammalian cardiac regeneration and uncover a targetable mechanometabolic pathway for cardiac repair.

Introduction

The adult mammalian heart sustains lifelong contractile work but has little capacity to regenerate after injury[1,2]. By contrast, neonatal CMs can re-enter the cell cycle and rebuild damaged myocardium during a brief postnatal window, before this regenerative competence is rapidly lost[3-6]. This transition coincides with CM maturation, during which cells acquire organized sarcomeres, efficient excitation–contraction coupling, robust Ca^{2+} cycling and increased contractile force[7-9]. Although many molecular pathways have been implicated in CM proliferation[2,10-16], why the acquisition of mature cardiac function is coupled to regenerative arrest remains poorly understood.

Contractility is one of the defining features of postnatal CM maturation[17]. Mature CMs continuously convert electrical excitation and Ca^{2+} transients into mechanical force, whereas regenerative CMs often display partial dedifferentiation, sarcomere remodeling and altered Ca^{2+} handling[8,9,18]. These observations raise a fundamental question: does the mature contractile state merely mark the loss of regenerative capacity, or does it actively restrain CM plasticity? Direct evidence that contractile homeostasis functions as an instructive barrier to cardiac regeneration has been lacking.

Mechanical forces are increasingly recognized as regulators of cellular metabolism and fate[19-21]. In many tissues, mechanotransduction reshapes metabolic pathways to control proliferation, differentiation, and adaptation[21]. The heart is an especially force-generating organ, and CM maturation is accompanied by coordinated changes in contractile function and metabolism[22,23]. However, whether contractile activity is converted into specific metabolic signals that regulate CM regenerative competence remains unknown.

Here we identify a KLF3-controlled mechanometabolic circuit that links CM

contractile homeostasis to regenerative arrest. We show that KLF3 is induced during postnatal maturation and directly represses genes involved in Ca^{2+} handling and excitation–contraction coupling. CM-specific *Klf3* deletion enhances Ca^{2+} cycling and contractility, increases membrane mechanical stress, activates neutral sphingomyelinase-dependent sphingolipid remodeling and promotes LacCer accumulation. This pathway reactivates CM proliferation and improves cardiac repair after MI. These findings establish contractile homeostasis as an active maturation-linked barrier to mammalian heart regeneration and reveal a targetable mechanometabolic pathway for cardiac repair.

Results

KLF3 restrains the postnatal contractile programme to maintain CM homeostasis

Transcriptional control is central to CM maturation[8,10], but the factors that couple maturation-associated contractile function to regenerative arrest remain incompletely defined. To identify transcription factors underlying this transition, we first analyzed the postnatal expression dynamics of genes involved in cardiac contraction and Ca^{2+} handling (Extended Data Fig. 1a). Motif enrichment analysis nominated KLF3 as a candidate regulator of the maturation-associated contractile programme (Extended Data Fig. 1b, c). Consistent with this nomination, Klf3 mRNA and KLF3 protein increased progressively during postnatal heart development, with marked enrichment in mature myocardium compared with neonatal hearts (Fig. 1a,b). Together with previous evidence that KLF3 is expressed in striated muscle and regulates muscle-specific gene expression[24,25], these observations suggest that KLF3 may contribute to the establishment of the mature CM state.

KLF3 has been characterized as a CtBP-associated transcriptional repressor[26], but its function in postnatal CMs remains poorly understood. We next asked whether KLF3

activates or restrains the maturation-associated contractile programme. We generated CM-specific *Klf3* knockout mice by crossing $Klf3^{fl/fl}$ mice with *Ckm-Cre* transgenic mice ($Ckm^{cre/+}$; $Klf3^{fl/fl}$, hereafter *Klf3*-cKO), with littermate $Ckm^{+/+}$; $Klf3^{fl/fl}$ serving as controls (Ctrl) (Fig. 1c). Efficient recombination was detected from P14 onward, and resulted in robust reductions of Klf3 mRNA and KLF3 protein in adult CMs (Fig. 1d,e and Extended Data Fig. 2a). *Klf3*-cKO mice developed normally, and histological analyses from embryonic day 18 (E18) to adulthood (3M) revealed no overt abnormalities in cardiac morphology, chamber structure or myocardial architecture (Fig. 1f and Extended Data Fig. 2b-e). Consistently, ECHO of 3-month-old mice showed preserved left ventricular ejection fraction, fractional shortening, and wall thickness under basal conditions (Fig. 1g,h and Extended Data Fig. 2f,g). Thus, KLF3 is dispensable for gross cardiac development and resting systolic function.

Despite this apparently normal baseline phenotype, *Klf3*-cKO mice displayed a significantly increased heart rate (Fig. 1i), suggesting altered regulation of CM excitability or contractile activity. To investigate the underlying transcriptional changes, we performed RNA sequencing of CMs isolated from adult control and *Klf3*-cKO hearts. *Klf3* deletion caused broad transcriptional remodeling (Fig. 1j and Extended Data Fig. 3a), with upregulation of genes involved in cardiac muscle contraction, sarcoplasmic reticulum Ca^{2+} transport, ATP metabolism, mitochondrial respiration, and oxidative phosphorylation (Fig. 1k and Extended Data Fig. 3b,c). By contrast, genes associated with extracellular matrix organization, cytoskeletal assembly and inflammatory responses were reduced (Fig. 1l). These data indicate that loss of *Klf3* activates a coordinated contractile, Ca^{2+}-handling, and energetic programme in adult CMs.

We next asked whether these transcriptional changes altered intrinsic CM function. Measurements of isolated adult CMs using the IonOptix system revealed increased

sarcomere shortening and accelerated contraction and relaxation kinetics in *Klf3*-deficient cells (Fig. 1m,n). Ca^{2+} imaging further showed enhanced Ca^{2+} transient amplitude together with faster Ca^{2+} release and decay (Fig. 1o,p). In parallel, Seahorse analyses revealed increased oxidative phosphorylation and glycolytic capacity (Extended Data Fig. 3d-g), consistent with the higher energetic demand imposed by enhanced contractile activity. Thus, *Klf3* loss shifts adult CMs into a hypercontractile and metabolically active state characterized by augmented Ca^{2+} cycling and contractile output.

To determine whether KLF3 directly controls this programme, we performed CUT&Tag profiling in adult CMs. KLF3 occupancy was enriched at promoter-proximal regions surrounding transcription start sites (Fig. 1q). Differential binding analysis between control and *Klf3*-cKO CMs identified high-confidence KLF3-dependent peaks whose associated genes were strongly enriched for heart contraction, regulation of heart rate, sarcomere organization, sarcoplasmic reticulum Ca^{2+} transport and glycolytic metabolism (Fig. 1r). KLF3 directly occupied regulatory regions of multiple genes encoding contractile and Ca^{2+}-handling components, including *Myh6*, *Ttn*, *Tcap*, *Ryr2*, *Cacna1c*, *Atp2a2*, *Pln*, and *Hrc*. Integration of CUT&Tag and RNA-seq further showed that these KLF3-bound genes were upregulated after *Klf3* deletion (Fig. 1s,t and Extended Data Fig. 3h-n). These findings indicate that KLF3 directly represses a maturation-associated contractile and Ca^{2+}-handling gene module to maintain CM contractile homeostasis. Thus, KLF3 is induced during maturation not to initiate the contractile programme, but to constrain it within a homeostatic range.

Klf3 loss reactivates CM proliferative competence

Having shown that KLF3 is induced during postnatal CM maturation, we next examined whether it is suppressed during regenerative activation. In neonatal hearts

subjected to apical resection (AR), KLF3 protein abundance was markedly reduced in CMs from the regenerative region compared with sham-operated controls (Extended Data Fig. 4a-d). This reciprocal regulation suggested that KLF3 might function as a maturation-linked brake on CM plasticity and proliferation.

To test this possibility, we used adenoviral shRNA to knock down Klf3 in primary neonatal mouse CMs. Klf3 knockdown significantly increased the proportion of Ki67-positive and Aurora B-positive CMs (Fig. 2a,b and Extended Data Fig. 5a), indicating enhanced cell-cycle re-entry and mitotic progression. A similar response was observed in neonatal rat CMs (Extended Data Fig. 5b-d), suggesting that the anti-proliferative function of KLF3 is conserved across rodent CMs. Importantly, mosaic analysis with double markers (MADM), a genetic approach in which single-labelled CMs mark completed cytokinesis[27,28], further showed that Klf3 knockdown increased the fraction of single-labelled CMs (Fig. 2c). This genetic mosaic assay provides evidence for completion of cytokinesis, distinguishing Klf3 knockdown from mere activation of cell-cycle markers.

We next examined whether *Klf3* deletion reactivates CM proliferation in vivo. CMs were identified by cardiac troponin T (cTnT) staining, and proliferative events were quantified only within cTnT-positive cells. In *Klf3*-cKO hearts, Ki67-positive and Aurora B-positive CMs were significantly increased at postnatal day 24, a stage at which CM proliferative activity is normally low (Fig. 2d and Extended Data Fig. 5e). This proliferative response persisted into adulthood, as shown by the continued presence of Ki67-positive CMs in 3-month-old *Klf3*-cKO hearts (Fig. 2e). Thus, loss of *Klf3* is sufficient to sustain CM cell-cycle activity beyond the neonatal regenerative window.

Despite increased CM proliferation, *Klf3*-cKO hearts did not show overt

159 enlargement, suggesting that *Klf3* loss might alter CM growth state rather than simply
160 increasing organ size. Consistent with this possibility, wheat germ agglutinin (WGA)
161 staining revealed a significant reduction in CM cross-sectional area in *Klf3*-cKO hearts
162 (Fig. 2f). Isolated adult *Klf3*-deficient CMs also showed significantly reduced cell
163 length and surface area, whereas cell width was slightly decreased (Fig. 2g,h and
164 Extended Data Fig. 5f). These findings indicate that *Klf3* deletion shifts CMs away from
165 the hypertrophic growth state characteristic of mature myocardium.

166 Because postnatal CM maturation is associated with hypertrophic growth and
167 multinucleation[10,17], we next assessed nucleation status and CM number. *Klf3* deletion
168 increased the proportion of mononucleated CMs (Fig. 2i) and significantly increased
169 the total number of CMs per heart (Fig. 2j). These changes indicate that loss of *Klf3*
170 favors a less mature, proliferation-permissive CM state rather than merely inducing
171 transient cell-cycle marker expression. In agreement with this interpretation, adult *Klf3*-
172 cKO hearts showed sporadic re-expression of smooth muscle actin (Fig. 2k), a marker
173 normally suppressed in mature CMs. Western blot analysis further revealed increased
174 Cyclin E1 and reduced p21 (also known as CDKN1A), whereas Cyclin A2, Cyclin B1
175 and CDK1 were largely unchanged (Fig. 2l and Extended Data Fig. 5g), suggesting
176 preferential activation of G1/S entry.

177 Together, these findings identify KLF3 as a maturation-associated suppressor of
178 CM plasticity. Loss of *Klf3* partially reverses features of the mature CM state, reduces
179 hypertrophic growth, increases the mononucleated CM population and reactivates
180 proliferative competence in vivo.

181 ## *Klf3* suppression enhances post-infarction cardiac repair

182 Having shown that *Klf3* loss reactivates CM proliferative competence, we next
183 asked whether this response improves cardiac repair after injury. We induced MI in 3-

month-old *Klf3*-cKO mice and littermate controls by permanent ligation of the left anterior descending (LAD) coronary artery (Fig. 3a and Extended Data Fig. 6a). ECHO performed 7 days after infarction showed comparable reductions in ejection fraction and fractional shortening in control and *Klf3*-cKO mice, indicating similar initial injury severity (Fig. 3b,c). By 30 days after MI, however, control mice showed progressive deterioration of cardiac function, whereas *Klf3*-cKO mice maintained significantly better systolic performance (Fig. 3b,c). This functional benefit persisted at 67 days after injury (Fig. 3b,c and Extended Data Fig. 6b). Consistently, Masson's trichrome staining revealed reduced left ventricular fibrotic area in *Klf3*-cKO hearts, indicating attenuated adverse remodeling after MI (Fig. 3d,e).

We next examined whether improved repair was associated with increased CM cell-cycle activity. At 67 days after MI, *Klf3*-cKO hearts contained significantly more Ki67-positive and phospho-histone H3 (pH3)-positive CMs than control hearts (Fig. 3f,g). These findings indicate that *Klf3* deletion sustains CM cell-cycle re-entry and mitotic activity after injury, coinciding with improved structural and functional recovery.

To determine whether acute *Klf3* inactivation in the adult heart is sufficient to induce a regenerative-like state, we generated tamoxifen (TAM)-inducible CM-specific *Klf3* knockout (*Klf3*-iKO) mice (Fig. 3h). TAM administration in 3-month-old mice efficiently deleted *Klf3* without causing overt changes in cardiac morphology, heart size or resting systolic function, although heart rate was also modestly increased (Fig. 3i,j and Extended Data Fig. 6c-j). Adult-onset *Klf3* deletion reduced CM cross-sectional area and induced sporadic re-expression of smooth muscle actin (Fig. 3k,l), consistent with partial relaxation of the mature CM state. Importantly, inducible *Klf3* deletion increased the number of Ki67-positive and pH3-positive CMs (Fig. 3m,n),

demonstrating that suppression of KLF3 in mature CMs is sufficient to reactivate cell-cycle activity in vivo.

Finally, we tested whether *Klf3* inhibition after established injury could improve cardiac repair. TAM was injected i.p. 4 days after MI (Fig. 3o), allowing *Klf3* deletion to occur after the onset of adverse remodeling. Post-injury induction of *Klf3* deletion partially preserved systolic function after MI, with a consistent trend in ejection fraction and significant improvement in fractional shortening at later time points (Fig. 3p,q and Extended Data Fig. 6k). This was accompanied by a significant reduction in fibrotic scar formation (Fig. 3r and Extended Data Fig. 6l). These results indicate that adult-onset suppression of KLF3 can enhance recovery even when initiated after myocardial injury. Together, our data identify KLF3 as a CM-intrinsic brake on post-infarction repair and support transient KLF3 inhibition as a potential strategy to promote regenerative cardiac recovery.

Klf3 loss promotes a LacCer-enriched glycosphingolipid programme

The ability of *Klf3* loss to enhance contractile activity, energetic demand and CM proliferation raised the possibility that metabolic pathways may transduce changes in functional state into regenerative signals. To identify such downstream programmes, we integrated RNA-seq with untargeted metabolomic profiling of isolated adult CMs from control and *Klf3*-cKO hearts. Consistent with significant upregulation of genes involved in precursor metabolite generation, energy production, and mitochondrial metabolism, a broad metabolic shift was observed after *Klf3* deletion (Fig. 4a, b). Pathway analysis of differentially abundant metabolites, together with transcriptome–metabolome integration, identified sphingolipid metabolism as the most prominent metabolic programme altered by *Klf3* loss (Fig. 4c-e). Similarly, sphingolipid metabolism was also significantly changed in *Klf3*-iKO hearts (Extended Data Fig. 7a-

d).

Because sphingolipid metabolism has been implicated in neonatal cardiac regeneration[29], we examined individual lipid species altered in *Klf3*-deficient CMs. Untargeted metabolomics identified LacCer as a prominently enriched metabolite (Extended Data Fig. 8a), and targeted lipidomic analysis confirmed a significant increase in LacCer abundance in adult *Klf3*-deficient CMs (Fig. 4f). These findings indicate that KLF3 loss prominently enhances glycosphingolipid accumulation, with LacCer representing a major lipid species induced in *Klf3*-deficient CMs.

To understand how KLF3 controls LacCer production, we first analyzed genes involved in sphingolipid metabolism. *Klf3* deletion was associated with coordinated upregulation of sphingolipid biosynthetic genes and reduced expression of genes involved in sphingolipid degradation (Extended Data Fig. 8b,c). Thus, KLF3 loss drives sphingolipid metabolism towards an anabolic glycosphingolipid programme.

We next asked whether this metabolic shift involved direct transcriptional regulation by KLF3. Interrogation of the KLF3 CUT&Tag dataset revealed KLF3 occupancy at the promoter region of *B4galt6* (Fig. 4g), which encodes a glycosyltransferase that converts glucosylceramide to LacCer[30]. Consistent with direct repression, B4GALT6 protein abundance was markedly increased in *Klf3*-deficient CMs (Fig. 4h,i). These results suggest that KLF3 may limit LacCer biosynthesis in part by repressing *B4galt6*.

Notably, LacCer accumulated at the plasma membrane of *Klf3*-deficient CMs and was accompanied by increased ERK1 phosphorylation (Fig. 4j and Extended Data Fig. 8d), consistent with previous reports that LacCer can activate ERK-associated mitogenic signaling[31,32]. We then tested whether LacCer is sufficient to promote CM proliferative activity. Exogenous LacCer treatment increased Aurora B-positive and

Ki67-positive CMs in a dose-dependent manner, with 0.5 μM producing the strongest response (Fig. 4k,l). Together, these findings identify LacCer as a bioactive downstream effector of KLF3 loss that is sufficient to promote CM cell-cycle re-entry.

Collectively, these data show that KLF3 restrains a pro-regenerative sphingolipid programme in CMs.

Contractile stress activates nSMase-dependent sphingolipid signaling

Klf3 loss increased Ca^{2+} cycling and contractile activity while promoting LacCer accumulation, raising the possibility that altered mechanical activity contributes to sphingolipid remodeling. Neutral sphingomyelinase (nSMase) responds to membrane mechanical stress and catalyses the conversion of sphingomyelin to ceramide (Cer)[33,34], an upstream precursor for complex sphingolipid synthesis. Consistent with this, Cer was significantly increased in *Klf3*-cKO CMs (Fig. 5a). We therefore asked whether the hypercontractile state induced by *Klf3* deletion activates nSMase-dependent sphingolipid signaling in CMs.

To assess membrane mechanical stress, we used the mechanosensitive probe Flipper-TR[35]. Fluorescence lifetime imaging revealed increased Flipper-TR lifetime in *Klf3*-deficient CMs (Fig. 5b), indicating elevated plasma membrane tension after *Klf3* deletion. We next monitored nSMase activity using BODIPY-labelled sphingomyelin. In control CMs, BODIPY fluorescence was mainly retained at the plasma membrane (Fig. 5c). By contrast, *Klf3*-deficient CMs showed redistribution of the signal from the membrane to the cytoplasm, consistent with enhanced conversion of membrane-associated sphingomyelin to ceramide[36] (Fig. 5c). This redistribution was prevented by the nSMase inhibitor GW4869 or by lowering extracellular Ca^{2+} (Fig. 5c), indicating that nSMase activation depends on Ca^{2+}-driven contractile activity. Targeted lipid analysis further showed that *Klf3* deletion increased Cer abundance under physiological

284 Ca^{2+} conditions, whereas this increase was largely abolished by GW4869 or low- Ca^{2+}
285 treatment (Fig. 5d).

286 We next tested whether nSMase activation is required for the proliferative response
287 induced by *Klf3* loss. *Klf3* deletion increased the proportion of Aurora B-positive and
288 Ki67-positive CMs, but both responses were abolished by GW4869 or low-Ca^{2+}
289 conditions (Fig. 5e,f). These results indicate that Ca^{2+}-dependent contractile activity
290 and nSMase-mediated sphingomyelin hydrolysis are required for CM cell-cycle re-
291 entry after KLF3 loss.

292 To determine whether enhanced contractile activity is sufficient to engage this
293 pathway independent of *Klf3* deletion, we pharmacologically manipulated CM
294 contraction[37]. Isoproterenol increased membrane mechanical stress, activated nSMase,
295 and increased Aurora B-positive and Ki67-positive CMs (Fig. 5g-j). These effects were
296 abolished by GW4869, indicating that the proliferative response to contractile
297 stimulation requires nSMase activity. Thus, perturbing contractile homeostasis is
298 sufficient to activate an nSMase-dependent sphingolipid programme that promotes CM
299 cell-cycle re-entry.

300 **LacCer is sufficient to enhance post-infarction cardiac repair**

301 Having identified LacCer as a downstream effector of *Klf3* loss and contractility-
302 dependent sphingolipid signaling, we next asked whether LacCer is sufficient to
303 improve cardiac repair after injury. To this end, we administered LacCer at multiple
304 time points after MI and monitored cardiac function by serial ECHO (Fig. 6a).
305 Compared with vehicle-treated mice, LacCer-treated mice showed attenuated
306 deterioration of systolic function after infarction, with improved ejection fraction and
307 fractional shortening (Fig. 6b-d). LacCer treatment also reduced left ventricular dilation,
308 indicating mitigation of adverse post-infarction remodeling (Fig. 6e,f).

Histological analysis further supported a protective effect of LacCer after injury. Masson's trichrome staining revealed reduced fibrotic remodeling in LacCer-treated hearts compared with vehicle-treated controls (Fig. 6g,h). Together with the ability of LacCer to stimulate CM cell-cycle re-entry in vitro, these findings indicate that LacCer is sufficient to enhance post-infarction cardiac repair. Thus, the KLF3-regulated mechanometabolic pathway converges on a bioactive sphingolipid signal that can be pharmacologically supplied to improve cardiac recovery after MI.

Discussion

In this study, we identify contractile homeostasis as an active, cell-intrinsic barrier to mammalian cardiac regeneration. KLF3 is induced during postnatal CM maturation and maintains the mature contractile state by repressing genes involved in Ca^{2+} handling and excitation–contraction coupling. Its loss enhances Ca^{2+} cycling and contraction, increases membrane mechanical stress, activates neutral sphingomyelinase-dependent sphingolipid remodeling and promotes LacCer accumulation. These changes reactivate CM proliferative competence and improve cardiac repair after MI. Thus, mature contractile function is not simply a consequence of CM maturation, but an instructive state that limits regenerative plasticity through a mechanometabolic circuit.

This finding reframes the link between CM maturation and regenerative arrest. The postnatal heart becomes optimized for continuous mechanical work, but this specialization coincides with cell-cycle withdrawal. Our data suggest that these processes are mechanistically coupled: the contractile programme that enables adult pump function also establishes a lipid-metabolic state that restrains regenerative plasticity. KLF3 provides a molecular entry point into this checkpoint by maintaining Ca^{2+}–contractile homeostasis and repressing glycosphingolipid biosynthesis. Its loss relaxes the mature CM state through two convergent mechanisms: increased contractile

stress, which activates nSMase, and a transcriptional shift in glycosphingolipid biosynthesis marked by B4galt6 derepression and LacCer accumulation. Sphingolipid metabolism has recently been implicated in mammalian heart regeneration through the SphK2–S1P branch[29]. Our study identifies contractile activity and membrane tension as upstream inputs into a distinct nSMase–LacCer branch, thereby linking excitation–contraction homeostasis to regenerative lipid signaling.

The identification of LacCer as a bioactive output of this circuit links functional maturation to a targetable metabolic signal. Exogenous LacCer promoted CM cell-cycle re-entry and improved post-infarction cardiac repair, suggesting that transient activation of contractility-linked sphingolipid signaling may be sufficient to enhance cardiac recovery. More broadly, this work raises the possibility that specialized physiological functions can impose metabolic barriers to regeneration in mature mammalian tissues. Whether similar function-coupled mechanometabolic checkpoints operate in other low-regenerative tissues remains an important question.

Several issues remain unresolved. The molecular mechanism by which nSMase senses contractile membrane stress is unknown, and LacCer probably acts together with ceramide and other sphingolipid species rather than as an isolated signal. It will also be important to determine whether transient relaxation of contractile homeostasis can be achieved safely without compromising long-term myocardial function. Nevertheless, our findings provide a framework connecting functional maturation, mechanotransduction, lipid metabolism and regenerative competence, and suggest a strategy for promoting cardiac repair by targeting the contractility–sphingolipid axis.

Methods

Animals and ethical approval

All animal experiments were performed in accordance with institutional guidelines and were approved by the Animal Care and Use Committee of Peking University, Beijing, China, under protocol number [IMM-WangYM-1]. Mice were maintained in a specific pathogen-free animal facility under a 12 h light/dark cycle at 20−26°C and humidity of 30−70%, with free access to standard chow and water. Both male and female animals were used unless otherwise stated. *Klf3*$^{fl/fl}$ mice were generated by inserting loxP sites flanking exons 3 and 4 of the *Klf3* locus using CRISPR-Cas9-mediated genome editing. CM-specific *Klf3* knockout mice were generated by crossing *Klf3*$^{fl/fl}$ mice with *Ckm*-Cre mice (*Ckm*$^{cre/+}$)[38]. *Ckm*$^{cre/+}$;*Klf3*$^{fl/fl}$ mice are referred to as *Klf3*-cKO mice, and littermate *Ckm*$^{+/+}$;*Klf3*$^{fl/fl}$ mice were used as controls. Inducible CM-specific *Klf3* knockout mice were generated by crossing *Klf3*$^{fl/fl}$ mice with *Myh6*-MerCreMer mice[39]. *Myh6*$^{MCM/+}$;*Klf3*$^{fl/fl}$ mice are referred to as *Klf3*-iKO mice, and *Myh6*$^{MCM/+}$;*Klf3*$^{+/+}$ littermates were used as controls where indicated. For inducible deletion, TAM was dissolved in corn oil and administered by intraperitoneal (i.p.) injection at 75 mg kg^{-1} for seven doses. The injection schedule was daily for 7 consecutive days. Mice were analyzed at the indicated time points after TAM withdrawal. *MADM-ML-11*$^{TG/GT}$ mice were generated by crossing homozygous *MADM-ML-11*$^{TG/TG}$ and *MADM-ML-11*$^{GT/GT}$ mice[27,40]. Wild-type C57BL/6J mice and Sprague–Dawley rats were purchased from Beijing Vital River Laboratory Animal Technology (Beijing). Genotyping was performed using genomic DNA extracted from tail biopsies. PCR primers and expected product sizes are listed in Supplementary Table 1.

Randomization, blinding and exclusion criteria

For animal treatment studies, mice were randomly assigned to experimental groups after genotype confirmation. For MI and LacCer treatment experiments, allocation to treatment groups was performed using cage-balanced randomization. Investigators performing echocardiography, histological quantification, immunofluorescence (IF) imaging and image analysis were blinded to genotype and treatment whenever possible. Pre-established exclusion criteria for MI experiments included perioperative death, failed coronary ligation, absence of left ventricular wall-motion abnormality after surgery, lack of myocardial blanching during ligation, poor echocardiographic image quality, or technical failure during tissue processing. Exact numbers of animals included, excluded, and lost after surgery are reported in Supplementary Table 2. No statistical methods were used to predetermine sample size. Sample sizes were chosen based on previous studies, pilot experiments and expected variability of MI and CM proliferation assays.

Neonatal CM isolation

Neonatal mouse and rat CMs were isolated from postnatal day P6 hearts and P2 hearts. Neonates were sterilized with 75% ethanol, and hearts were rapidly excised after thoracic incision. Ventricular tissue was minced into～1 mm^3 fragments and digested in 0.5 ml of D-Hanks buffer (Solarbio, H1040) containing 0.1% trypsin and 0.05% type II collagenase (Sigma, V900892) at 37°C for 5 min. After natural sedimentation, the supernatant was discarded. Fresh enzyme solution was added, gently agitated, and incubated for 6 min with inversion every 2 min. Digestion was repeated for 10 times. The cell suspension was collected into equal volume of medium containing 10% FBS (Gibco, 10099141) to terminate enzymatic activity. All collected cell suspensions were filtered through a 100 μm mesh, centrifuged at 170 *g* for 5 min, and resuspended in

culture medium. To reduce non-CM contamination, cells were pre-plated for 120 min at 37°C. The non-adherent CM-enriched fraction was collected and cultured for 48 h in plating medium consisting of DMEM medium containing 7% FBS. 20 μM cytosine arabinoside (TargetMol, T1272) was added to suppress non-myocyte proliferation. All CMs, except those used for the nSMase activity assay, were cultured in culture medium consisting of DMEM supplemented with 2% FBS, 1×NEAA (ThermoFisher, 11140050), 1×Glutamax (ThermoFisher, 35050061) and 1×Penicillin/Streptomycin (Sigma, P4333).

Adult CM isolation

Adult CMs were isolated using a modified Langendorff-free enzymatic dissociation method as described previously[41], with minor modifications. Three-month-old mice were anesthetized with 1.25% tribromoethanol (20 ml kg^{-1}, i.p.), disinfected with 75% ethanol, and transferred to a biosafety cabinet. After thoracotomy, the descending aorta was severed, and the heart was perfused through the right ventricle with 10 ml of EDTA buffer containing 5 mM KCl, 130 mM NaCl, 10 mM HEPES, 0.5 mM NaH_2PO_4, 10 mM 2, 3-butanedione monoxime (BDM, Sigma-Aldrich, 31550), 5 mM EDTA, 10 mM glucose, and 10 mM taurine (Sigma-Aldrich, V900296). The cardiac apex was then clamped, and the heart was excised and sequentially perfused through the left ventricle with 5 ml EDTA buffer followed by 5 ml perfusion buffer of identical composition except for the omission of EDTA. Enzymatic digestion was performed using pre-warmed collagenase buffer containing 0.05% collagenase II, 0.05% collagenase IV, 0.005% protease XIV until the myocardium became visibly softened. Ventricular tissue was minced, gently triturated, and filtered through a 150 μm mesh. Digestion was terminated by adding an equal volume of perfusion buffer containing 5% FBS. CMs were collected by centrifugation at 20 *g* for 2 min, gradually reintroduced to Ca^{2+}, and

resuspended in plating medium consisting of M199 supplemented with 5% FBS and 10 mM BDM. CMs were then seeded onto Laminin (Thermo Fisher, 23017-015) -coated plates (10 μg ml^{-1}). After 12 h, the medium was replaced with culture medium of M199 supplemented with 5% BSA, 1× ITS, 1× CD lipid, and 10 mM BDM. For RNA-seq, CUT&Tag and metabolomics analyses, freshly isolated CMs were subjected to two rounds of low-speed centrifugation (20 *g* for 2 min each) to obtain highly purified, rod-shaped adult CMs.

Neonatal apical resection

Neonatal mouse heart AR was performed within 1～2 days after birth as described previously[3], with minor modifications. Pups were placed on ice for 2 min to induce hypothermic anesthesia. After complete cessation of movement, the chest and abdomen were disinfected with 75% ethanol. A small left thoracotomy was made at the fourth intercostal space using fine scissors to expose the beating heart. Approximately 10−15% of the ventricular apex was excised with micro-scissors under a stereomicroscope. Hemostasis was achieved by gentle compression with a sterile cotton swab until bleeding stopped. The ribs, muscle, and skin were closed sequentially with 6−0 absorbable sutures. After surgery, pups were placed on a 37°C-heating pad for recovery and returned to their mothers once spontaneous movement resumed. Sham-operated pups underwent the same procedure without apical resection.

Myocardial infarction

MI was induced in 3-month-old mice by permanent ligation of the left anterior descending coronary artery (LAD)[42]. Mice were anesthetized via i.p. injection of 1.25% tribromoethanol (20 ml kg^{-1}). The chest and neck were disinfected with 75% ethanol, and mice were secured in a supine position. A ～2 cm incision was made along the

neck and the left side of the chest to expose the trachea and thoracic cavity. After blunt dissection of the overlying muscle, mice were orally intubated and connected to a small-animal ventilator. Adequate ventilation was confirmed by synchronized thoracic excursion. Electrocardiogram (ECG) electrodes were attached to the left forelimb, left hindlimb, and right hindlimb for continuous monitoring. Left thoracotomy was performed by separating the intercostal muscles between the second and third ribs, and the thoracic cavity was opened using a chest expander to expose the heart. After removal of the pericardium, the LAD was permanently ligated using a 6−0 non-absorbable suture. Successful ligation was verified by immediate ST-segment elevation on the ECG. The thoracic cavity was closed in layers with 5−0 sutures. Residual air was evacuated to restore negative intrathoracic pressure, and the muscle and skin were sutured to complete the procedure. Mice were maintained on a warming pad until recovery and monitored postoperatively. Sham-operated mice underwent the same procedure except that the LAD was not ligated. Mice with perioperative death, failed LAD ligation or poor postoperative recovery were excluded according to pre-established criteria and reported in Supplementary Table 2.

CM number, nucleation, and size

Dissected adult hearts were rinsed in ice-cold PBS and fixed overnight in 4% paraformaldehyde (PFA) for CM number quantification. After washing with PBS, hearts were minced into 1−3 mm^3 fragments and subjected to enzymatic digestion at 37°C in digestion buffer (PBS containing 0.05% collagenase II and 0.05% collagenase IV) with constant agitation. At 12 h intervals, dissociated CMs were collected by centrifugation at 20 *g* for 2 min, and the remaining tissue fragments were replenished with fresh digestion buffer until complete dissociation. Collected CMs were then

pelleted at 20 *g* for 2 min and counted using a hemocytometer. Following cell counting, isolated adult CMs were immunostained for cTnT and DAPI to assess CM nucleation. CM length and width were measured using Fiji (ImageJ, NIH).

Quantitative RT–PCR

Total RNA was extracted using TRNzol reagent (TIANGEN, DP424) according to the manufacturer's instructions. RNA was reverse-transcribed using HiScript III Q RT SuperMix (Vazyme, R323). Quantitative PCR was performed using SYBR Green Master Mix (Vazyme, Q141). Relative gene expression was calculated using the ΔΔCt method and normalized to Actb. Primer sequences are listed in Supplementary Table 1.

Western blot assays

Fresh mouse heart tissue was minced into ～1 mm^3 fragments and lysed in RIPA buffer supplemented with protease inhibitors. Samples were homogenized using a tissue grinder and incubated on a low-temperature rotator for 1 h to ensure complete protein extraction. Lysates were centrifuged at 13,000 rpm for 5 min at 4°C, and the supernatant was collected after removal of any floating lipid layer. Protein concentration was measured using a BCA Protein Assay Kit (Invitrogen, A65453). For SDS–PAGE, approximately 30 μg of total protein was mixed with SDS loading buffer and denatured at 99°C for 5 min. Proteins were separated by SDS–PAGE, transferred to PVDF membranes, and incubated with specific primary antibodies followed by corresponding secondary antibodies. Primary antibodies included anti-KLF3 (homemade rabbit polyclonal antibody produced by Biodragon, targeting mouse 14～231aa)[25], anti-KLF3 (Invitrogen, PA5111293), anti-HSP90β (Beyotime, AF0192), anti-ERK (CST, 9102), anti-Phospho-ERK (CST, 9101), anti-B4GALT6 (Novus, NBP1-69019), anti-CDK1 (Proteintech, 10762-1-AP), anti-Cyclin B1 (Proteintech, 67686-1-lg), anti-Cyclin D1

(CST, 55506), anti-Cyclin A2 (CST, 4656), anti-Cyclin E1 (CST, 20808), and anti-p21$^{Waf1/Cip1}$ (Beyotime, AF5252). Signals were acquired using a two-color infrared imaging system (Odyssey, LI-COR) and quantified using ImageJ (1.49v).

Histology and immunofluorescence

Mouse hearts were fixed in 4% PFA for 48 h, embedded in paraffin and cut into six transverse segments from the infarct site to the apex. Each block was sectioned at 8 μm. Paraffin sections were stained with Masson's trichrome and hematoxylin and eosin (H&E) using standard protocols. Cardiac scar size was quantified by ImageJ using the infarct midline-length method as described previously[43]. For IF, paraffin sections were incubated at 58°C for 30 min, deparaffinized, and subjected to microwave antigen retrieval in trisodium citrate buffer. After cooling to room temperature (RT), sections were permeabilized with PBST containing 0.5% Triton X-100 for 10 min and blocked with 4% FBS and 1% BSA for 1 h. Sections were incubated overnight at 4°C with primary antibodies diluted in blocking buffer. Primary antibodies included anti-cTnT (Invitrogen, MA5-12960), anti-Ki67 (Abcam, ab15580), anti-Aurora B (Abcam, ab2254), WGA-AF488 (Invitrogen, W11261), anti-αSMA (Abcam, ab124964), anti-phospho-Histone H3 (CST 9701), anti-Sarcomeric-α-Actinin (Abcam, ab317695), and anti-LacCer (Novus, NBP2-45291). Sections were then incubated with species-appropriate fluorescent secondary antibodies for 1 h at RT in the dark. Secondary antibodies included Alexa Fluor 488 Goat anti-rabbit (Invitrogen, A11008), Alexa Fluor 594 Goat anti-mouse (Invitrogen, A11005), and Alexa Fluor 647 Goat anti-mouse (Invitrogen, A21235). Nuclei were counterstained with DAPI (Sigma, D9542), and slides were mounted using antifade mounting medium. Images were acquired using a Leica high-speed spinning-disk confocal microscope and analyzed with ImageJ.

Echocardiography (ECHO)

ECHO was performed at defined time points before and after MI. Mice were anesthetized with 1% isoflurane following chest and abdominal hair removal. Cardiac structure and function were assessed using a Vevo 2100 high-resolution echocardiography (VisualSonics). B-mode imaging was used to evaluate left ventricular wall integrity and chamber dilation. M-mode imaging was used to measure ejection fraction, fractional shortening, left ventricular anterior and posterior wall thickness (LVAW, LVPW), and left ventricular internal diameter (LVID) during diastole and systole. All measurements, including heart rate, were obtained from three consecutive cardiac cycles, and averaged for analysis. EF and FS were calculated using standard equations as previously described[44]. All ECHO acquisition and analyses were performed in a blinded manner.

RNA sequencing and analysis

Adult mouse CMs were isolated using a Langendorff-free method, and total RNA was extracted using TRNzol. RNA integrity was assessed using an Agilent 2100 Bioanalyzer (Agilent), and only samples with an RNA integrity number $\geqslant$ 7.0 were used for library preparation. For each sample, 500 ng RNA was used for library preparation with the Ribo-off rRNA Depletion Kit (Vazyme, N406). Libraries were sequenced on an Illumina NovaSeq 6000 (Novogene, China) platform to generate paired-end 150 nt reads, with an average of ~50 million reads per sample. Sequencing reads were processed using Trim Galore (v0.6.7) to remove low quality bases and adapter sequences. Processed reads were aligned to the mouse genome (mm10) using STAR (v2.7.10a) with GENCODE vM25 annotation. Raw counts were quantified using featureCounts from Subread v2.0.1. Differential expression analysis was performed using DESeq2 v1.36.0. Differentially expressed genes were defined as genes with

adjusted $P < 0.05$ and $|\text{Log}_2$ fold change$| > 1$. Gene ontology (GO) enrichment and Kyoto Encyclopedia of Genes and Genomes (KEGG) pathway analyses were performed using clusterProfiler v4.7.1.3, with significance defined as adjusted $P < 0.05$.

Motif enrichment analysis

To identify transcription factors associated with postnatal contractile and Ca^{2+}-handling genes, publicly available RNA-seq data were downloaded from the Gene Expression Omnibus (GEO; accession number GSE95762)[45]. Genes exhibiting postnatal maturation-associated expression changes were identified, and genomic regions spanning ±2 kb around TSS were subjected to motif enrichment analysis using HOMER. Enriched transcription factor motifs were ranked according to enrichment *P* values. Only transcription factors with average TPM > 1 were included in analysis. Genes related to postnatal contractile and Ca^{2+} handling programme and their expression levels are listed in Supplementary Table 3.

CUT&Tag and data analysis

Adult mouse CMs were isolated via Langendorff-free perfusion and proceeded for CUT&Tag library construction using the Hyperactive Universal CUT&Tag Assay Kit for Illumina Pro (Vazyme, TD904). A total of 1×10^5 CMs were used for nuclear isolation in Nuclei Extraction (NE) buffer. Isolated nuclei were subsequently incubated with Concanavalin A (ConA)-coated magnetic beads and a homemade anti-KLF3 antibody (1:50 dilution) overnight at 4°C. After primary antibody binding, nuclei–ConA bead complexes were incubated with secondary antibody and pA/G–Tn5 transposase. Tagmented DNA fragments were PCR-amplified and purified using a bead-based method. Library quality was assessed using a Bioanalyzer. Sequencing was performed on an Illumina platform to generate paired-end reads. Sequencing reads were

first processed using Trim Galore v0.6.7 and subsequently aligned to the mouse reference genome mm10 using Bowtie2 v2.4.5. Unmapped reads, non-uniquely mapped reads, and PCR duplicates were removed using Picard v2.27.4 and Samtools v1.15.1. KLF3 binding peaks were identified using MACS2 v2.2.6 callpeak with the following parameters: -B --nomodel --nolambda --extsize 200. Differential binding analysis was performed using DiffBind v3.8.4 to identify significant changes in KLF3–DNA interactions. Peak annotation was conducted using ChIPseeker v1.31.4. Genome browser tracks were generated using the Integrative Genomics Viewer (IGV, v2.16.1).

Adenoviral and AAV transduction

The shRNA-miR-30 cassette was cloned into the pAV-cTnT-IFP vector to drive cardiac-specific expression under the control of the cTnT promoter. The resulting construct was packaged into adenovirus or the cardiotropic AAV9 serotype as indicated. Primary CMs were infected with adenovirus at an MOI of 200 and harvested 72 h post-infection or with AAV9 at an MOI of 10^6 and harvested 9 days post-infection for further analysis. The shRNA sequences used to knock down Klf3 are included in Supplementary Table 4.

MADM analysis

Primary CMs isolated from P6 *MADM-ML-11*$^{TG/GT}$ mice were infected with a *cTnT-Cre* adenovirus to induce mosaic labelling and then transduced with AAV9 expressing *cTnT-Klf3*-shRNA or control shRNA. GFP- and RFP-labelled CMs were imaged using a Nikon fluorescence microscope. Complete cytokinesis was inferred from the generation of single-labelled GFP^+ or RFP^+ CMs among total MADM-labelled CMs. Quantification was performed by investigators blinded to treatment.

Seahorse extracellular flux analysis

OCR and ECAR were measured using a Seahorse XFe24 Analyzer (Agilent) according to the manufacturer's instructions. Seahorse XFe24 plates were coated with laminin (10 μg ml^{-1}) before cell seeding. Primary CMs were isolated from 3-month-old wild-type or *Klf3*$^{fl/fl}$ mice, gradually reintroduced to Ca^{2+} and counted using a hemocytometer. CMs were resuspended in plating medium and seeded at 5,000 cells per well. After attachment for 1 h at 37°C in 5% CO_2, cells were infected with *cTnT-Cre* adenovirus at an MOI of 200 for 72 h to induce *Klf3* deletion. Mitochondrial respiratory function was assessed using the XF Cell Mito Stress Test Kit (Agilent, 103015-100). Sensor cartridges were hydrated overnight in XF calibrant before the assay. On the day of measurement, assay medium was freshly prepared, and OCR was measured after sequential injection of oligomycin (2 μM), FCCP (2 μM) and rotenone/antimycin A (1 μM). Glycolytic function was evaluated using the XF Glycolysis Stress Test Kit (Agilent, 103020-100), and ECAR was measured after sequential injection of glucose (10 mM), oligomycin (1 μM) and 2-deoxyglucose (50 mM). OCR and ECAR values were normalized to total protein per well, determined by BCA assay. Data were analyzed using Wave software (Agilent).

Untargeted metabolomics

Adult CMs were isolated from control and *Klf3*-cKO mice, washed with ice-cold PBS and snap-frozen. Metabolites were extracted using methanol–acetonitrile–water, followed by vertexing, sonication, and protein precipitation at −20°C. After centrifugation, supernatants were dried under vacuum and reconstituted in 50% acetonitrile. Protein pellets were retained for BCA-based normalization. LC–MS analysis was conducted using an ACQUITY UPLC I-Class system (Waters) coupled to a Synapt G2-Si QTOF mass spectrometer (Waters). Samples (2 μL) were separated on

an HSS T3 column (1.7 μm, 2.1 × 150 mm; Waters) at 30°C using water (0.1% formic acid) and acetonitrile with a linear gradient (0-100% acetonitrile over 0–23 min). Data were acquired in both positive and negative ESI modes (m/z 50-1200). QC samples were intermittently injected to ensure stability. Raw data were processed using MS-DIAL. Metabolite annotation was performed by matching experimental data against the Human Metabolome Database (HMDB) and other relevant metabolite databases using accurate mass, retention time and MS/MS spectral information. Data were normalized to protein content and log-transformed. Differential metabolites were identified using multivariate and univariate statistical analyses with FDR correction. Metabolites with an adjusted P value < 0.05 and an absolute fold change > 1.5 were considered significantly altered. Pathway enrichment analyses were performed using KEGG.

Targeted lipidomic analysis

Targeted lipidomic analysis was performed using an ACQUITY UPLC I-Class system coupled to a Xevo TQ-S micro triple quadrupole mass spectrometer (Waters). Lipids were extracted from isolated CMs using an MTBE-based protocol in the presence of isotope-labelled internal standards. Cer and LacCer species were separated on an ACQUITY UPLC BEH Amide column (1.7 μm, 2.1×100 mm; Waters) and detected in positive ESI mode using multiple reaction monitoring (MRM). Authentic standards of Cer (d18:1/20:0) (MCE, HY-112016), LacCer (d18:1/16:0) (MCE, HY-153830) and LacCer (d18:1/20:0) (MCE, HY-153860) were used to confirm metabolite identity and optimize MRM transitions. Relative lipid abundances were normalized to isotope-labelled internal standards.

Integrated transcriptome–metabolome analysis

Pathways enriched in the RNA-seq and metabolomics datasets were integrated at the

KEGG pathway level. Shared pathways were identified by intersecting significantly enriched KEGG pathways from both datasets (FDR-adjusted $P < 0.05$ for each analysis). Pathway impact values for metabolomic data were calculated using MetaboAnalyst based on pathway topology analysis. Integrated pathway plots were generated using GraphPad Prism 9.

CM contractility and Ca^{2+} transient

Adult CM contractility was measured using the IonOptix system (IonOptix). Isolated CMs were placed in Tyrode's solution (Solarbio, T1426) at 37°C and field-stimulated (5 V, 4 ms) at a frequency of 1 Hz. Sarcomere shortening, contraction velocity and relaxation velocity were recorded and analyzed using IonWizard software. Only rod-shaped CMs with clear sarcomeres and stable pacing responses were included. For Ca^{2+} transient measurements, isolated CMs were loaded with 5 μM Fura-2 AM (Invitrogen, 65-0858-39) for 30 min at RT, followed by a 20 min de-esterification period. Fluorescence signals were collected at 340/385 nm and expressed as F/F_0. Data were analyzed using IonWizard software, with parameters including Ca^{2+} transient amplitude and time to peak determined by single-exponential fitting. Investigators were blinded to genotype during analysis.

Flipper-TR membrane mechanical stress imaging

Membrane mechanical stress was assessed using the mechanosensitive fluorescent probe Flipper-TR (Spirochrome, SC020). Primary CMs were isolated from P6 wild-type and *Klf3*$^{fl/fl}$ mice as described above and plated onto laminin-coated glass-bottom dishes. To induce *Klf3* deletion, *Klf3*$^{fl/fl}$ CMs were infected with adenoviruses expressing *cTnT-Cre* for 72 h. For pharmacological studies, CMs were treated with DMSO or 2 μM (-)-isoproterenol hydrochloride (ISO; MCE, HY-B1670A) for 48 h

before imaging. CMs were incubated with 1 μM Flipper-TR in complete culture medium for 15 min at 37℃. CMs were then washed twice with HBSS and maintained in phenol red-free imaging medium during acquisition. Fluorescence lifetime imaging microscopy (FLIM) was performed immediately after probe loading using a Leica TCS SP8 STED 3X microscope equipped with a FALCON FLIM module. Flipper-TR was excited with a pulsed white-light laser at 488 nm, and emission was collected between 575 and 625 nm. Mean fluorescence lifetime values (τ mean) were quantified from manually delineated regions of interest corresponding to the CM plasma membrane. Image acquisition and analysis settings were kept identical across all groups within each experiment.

nSMase activity assay

nSMase activity was assessed using BODIPY FL C_{12}-sphingomyelin (BODIPY-SM) (Invitrogen, D7711) with minor modifications. Primary CMs were isolated from P6 Wt and *Klf3*$^{fl/fl}$ mice. CMs were infected with *cTnT-Cre* adenovirus to induce *Klf3* deletion and with *cTnT-IFP*-AAV9 to fluorescently label CMs, and were analyzed 7 days after infection. To modulate contractile activity, CMs were incubated for 48 h in D-Hanks' solution containing physiological Ca^{2+} (1.8 mM), low Ca^{2+} (0.1 mM), or ISO (2 μM). The nSMase inhibitor GW4869 (20 μM) was added during the final 4 h before BODIPY-SM loading. Cells were then incubated with 5 μM BODIPY-SM in D-Hanks' solution supplemented with 5 μM BSA and 10 mM HEPES for 30 min at 4 °C in the dark, allowing probe incorporation into the plasma membrane while minimizing endocytosis. After three washes with pre-cooled HEPES/D-Hanks' solution, cells were transferred to 37 °C and incubated for 30 min in the dark to allow enzymatic hydrolysis. nSMase-mediated cleavage of BODIPY-SM generates fluorescent Cer, leading to redistribution of fluorescence from the plasma membrane to intracellular membrane

compartments. Fluorescence images were acquired using identical settings across experimental groups.

Pharmacological treatments in cultured CMs

For LacCer treatment, primary CMs were treated with LacCer (d18:1/16:0) at 0.1, 0.25, 0.5, 1 and 3 μM for 72 h. LacCer was dissolved in anhydrous ethanol before use. Vehicle controls contained the same final concentration of ethanol. For inhibition of nSMase activity in the BODIPY-SM assay, CMs were pretreated with GW4869 (20 μM) for 4 h before BODIPY-SM loading. For cell proliferation assays and targeted lipidomic analyses, CMs were treated with GW4869 (2 μM) for 72 h. To modulate contractility, CMs were treated with 2 μM ISO for 72 h. Low-Ca^{2+} conditions were established by culturing cells in medium containing 0.1 mM Ca^{2+}.

LacCer administration after MI

Three-month-old male C57BL/6J mice underwent permanent ligation of LAD to induce MI. Immediately after LAD ligation, LacCer (5 μM) or vehicle was administered by intramyocardial injection into the ischemic myocardium at 4–5 evenly distributed sites (total injection volume, 100 μL). Starting 1 week after MI, mice received i.p. injections of LacCer (5 μM, 500 μL per injection) or vehicle twice weekly until 9 weeks post-MI. LacCer was dissolved in anhydrous ethanol and diluted in sterile saline before use. Vehicle-treated mice received an equivalent volume of saline containing the same final concentration of ethanol. Cardiac function was assessed by ECHO before surgery and at 1, 3, 5, 7, and 9 weeks post-MI.

Statistics and reproducibility

All samples used for quantitative analyses included at least three independent biological

719 replicates; exact sample sizes are indicated in the figure legends. Data are presented as
720 mean ± s.e.m unless otherwise indicated. For comparisons between two groups, two-
721 sided unpaired Student's *t*-test was used. For comparisons among more than two groups,
722 one-way ANOVA followed by Dunnett's multiple-comparison test was used. For
723 experiments involving multiple groups across multiple time points, two-way ANOVA
724 followed by Dunnett's multiple-comparison test was used. Longitudinal data were
725 analyzed using a linear mixed-effects model with genotype, time, and their interaction
726 as fixed effects and mouse ID as a random effect. Sidak's multiple-comparison test was
727 used for pairwise comparisons at individual time points. Statistical significance was
728 defined as $P < 0.05$. Each experiment was performed with at least three independent
729 biological replicates unless otherwise indicated. Exact sample sizes, replicate
730 definitions and statistical tests are provided in the figure legends. For sequencing and
731 omics experiments, each biological replicate represents CMs isolated from an
732 independent animal. No statistical methods were used to predetermine sample size.

733 **Data availability**

734 RNA-seq and CUT&Tag datasets generated in this study have been deposited in the
735 Gene Expression Omnibus under accession code GSE338610. Metabolomics and
736 lipidomics datasets have been deposited in MetaboLights[46] under the Study ID
737 MTBLS15076. All relevant data are presented in this article and its supplementary
738 information. Source data are provided with this paper.

739 **Code availability**

740 No custom code was used in this study.

741

Materials availability

Klf3$^{fl/fl}$ mice, viral vectors, plasmids, and other unique materials generated in this study are available from the corresponding authors upon reasonable request and completion of a material transfer agreement. Commercial reagents are included in Methods.

Acknowledgements

We thank all members of the Wang Laboratory for critical discussion of the project. We thank Drs. Jingwei Xiong and Zihao Wang for providing *MADM-ML-11*$^{TG/TG}$ and *MADM-ML-11*$^{GT/GT}$ mice, and *cTnT-Cre* adenovirus. We thank Drs. Ruiping Xiao and Aibin He for providing *Ckm*$^{cre/+}$ and *Myh6*$^{MCM/+}$ mice. We would like to thank Ms. Xueting Sun and Xuelian Wang from the Pathology Center of the College of Future Technology at Peking University for their help with heart pathological sections and staining. We thank Dr. Xin Li from the Center for Quantitative Biology at Peking University for her guidance on confocal microscopy imaging. We thank Ms. Jing Ren from the Sample Processing and Model Animal Center of the National Biomedical Imaging Center, Peking University, for technical assistance with imaging. We thank Dr. Li Quan and Ms. Xiaochuan Li at the Metabolomics Core, College of Future Technology, Peking University, for their assistance with metabolomics and lipidomics analyses. This study was supported by the National Key Research and Development Program of China (2021YFA1100200 to Y.W.), and the National Natural Science Foundation of China (91940302, 32025007 and 32130017 to Y.W.; 82070294 and 81830072 to H.-Q.C).

Author contributions

Y.W. conceived the study. Y.W. and H.-Q.C. designed and supervised the study. K.-W.W. designed and performed most experiments. Y.-X.W. assisted with RNA-seq library

766 construction. G.X. and X.-H.L. performed bioinformatics analysis. S.-J.D. assisted with
767 ECHO measurements. Y.-H.Z. assisted with mouse husbandry and genotyping. K.-W.W.
768 and Y.W. wrote the manuscript with input from all authors. All authors analyzed and
769 discussed the data and approved the final manuscript.

770 **Competing interests**

771 The authors declare no competing interests.

772

References

1 Maroli, G. & Braun, T. The long and winding road of cardiomyocyte maturation. *Cardiovasc. Res.* **117**, 712-726 (2021).

2 Koopmans, T. & van Rooij, E. Molecular gatekeepers of endogenous adult mammalian cardiomyocyte proliferation. *Nat. Rev. Cardiol.* **22**, 857-882 (2025).

3 Porrello, E. R. *et al.* Transient regenerative potential of the neonatal mouse heart. *Science* **331**, 1078-1080 (2011).

4 Rolland, L. & Jopling, C. The multifaceted nature of endogenous cardiac regeneration. *Front. Cardiovasc. Med.* **10**, 1138485 (2023).

5 Senyo, S. E. *et al.* Mammalian heart renewal by pre-existing cardiomyocytes. *Nature* **493**, 433-436 (2013).

6 Bergmann, O. *et al.* Evidence for cardiomyocyte renewal in humans. *Science* **324**, 98-102 (2009).

7 Bergmann, O. *et al.* Dynamics of cell generation and turnover in the human heart. *Cell* **161**, 1566-1575 (2015).

8 Sakamoto, T. & Kelly, D. P. Cardiac maturation. *J. Mol. Cell. Cardiol.* **187**, 38-50 (2024).

9 Beisaw, A. & Wu, C. C. Cardiomyocyte maturation and its reversal during cardiac regeneration. *Dev. Dyn.* **253**, 8-27 (2024).

10 Padula, S. L., Velayutham, N. & Yutzey, K. E. Transcriptional regulation of postnatal cardiomyocyte maturation and regeneration. *Int. J. Mol. Sci.* **22**, 3288 (2021).

11 Kikuchi, K. & Poss, K. D. Cardiac regenerative capacity and mechanisms. *Annu. Rev. Cell Dev. Biol.* **28**, 719-741 (2012).

12 Hashimoto, H., Olson, E. N. & Bassel-Duby, R. Therapeutic approaches for cardiac regeneration and repair. *Nat. Rev. Cardiol.* **15**, 585-600 (2018).

13 Bangru, S., Diegmiller, R., Di Talia, S. & Poss, K. D. Signal control during tissue regeneration in adult animals. *Nat. Rev. Mol. Cell Biol.* **27**, 316-335 (2026).

14 Li, X. *et al.* Inhibition of fatty acid oxidation enables heart regeneration in adult mice. *Nature* **622**, 619-626 (2023).

15 Puente, B. N. *et al.* The oxygen-rich postnatal environment induces cardiomyocyte cell-cycle arrest through DNA damage response. *Cell* **157**, 565-579 (2014).

16 Bassat, E. *et al.* The extracellular matrix protein agrin promotes heart regeneration in mice. *Nature* **547**, 179-184 (2017).

17 Guo, Y. X. & Pu, W. L. T. Cardiomyocyte maturation new phase in development. *Circ. Res.* **126**, 1086-1106 (2020).

18 Benitah, J. P. *et al.* Local calcium dynamics and signalling in cardiomyocytes. *Nat. Rev. Cardiol.* 10.1038/s41569-026-01286-8 (2026).

19 Tranter, J. D., Kumar, A., Nair, V. K. & Sah, R. Mechanosensing in metabolism. *Compr. Physiol.* **14**, 5269-5290 (2024).

20 Crozet, F. & Levayer, R. Emerging roles and mechanisms of ERK pathway mechanosensing. *Cell. Mol. Life Sci.* **80**, 355 (2023).

21 Fabiano, E. D., Poole, J. M. & Reinhart-King, C. A. Mechanometabolism: recent findings on the

intersection of cell adhesion, cell migration, and metabolism. *Am. J. Physiol. Heart Circ. Physiol.* **328**, C1866-C1879 (2025).

22 Salameh, S., Ogueri, V. & Posnack, N. G. Adapting to a new environment: postnatal maturation of the human cardiomyocyte. *J. Physiol.* **601**, 2593-2619 (2023).

23 Li, Z. *et al.* Postnatal state transition of cardiomyocyte as a primary step in heart maturation. *Protein Cell* **13**, 842-862 (2022).

24 Himeda, C. L., Ranish, J. A., Pearson, R. C., Crossley, M. & Hauschka, S. D. KLF3 regulates muscle-specific gene expression and synergizes with serum response factor on KLF binding sites. *Mol. Cell Biol.* **30**, 3430-3443 (2010).

25 Hao, J. *et al.* KLF3 promotes the 8-cell-like transcriptional state in pluripotent stem cells. *Cell Prolif.* **53**, e12914 (2020).

26 Turner, J., Nicholas, H., Bishop, D., Matthews, J. M. & Crossley, M. The LIM protein FHL3 binds basic Kruppel-like factor/Kruppel-like factor 3 and its co-repressor C-terminal-binding protein 2. *J. Biol. Chem.* **278**, 12786-127895 (2003).

27 Zong, H., Espinosa, S., Su, H. H., Muzumdar, M. D. & Luo, L. Q. Mosaic analysis with double markers in mice. *Cell* **121**, 479-492 (2005).

28 Ali, S. R. *et al.* Existing cardiomyocytes generate cardiomyocytes at a low rate after birth in mice. *Proc Natl Acad Sci U S A* **111**, 8850-8855 (2014).

29 Ji, X. Q. *et al.* Sphingolipid metabolism controls mammalian heart regeneration. *Cell Metab.* **36**, 839-856 (2024).

30 Tokuda, N. *et al.* beta4GalT6 is involved in the synthesis of lactosylceramide with less intensity than beta4GalT5. *Glycobiology* **23**, 1175-1183 (2013).

31 Chatterjee, S., Balram, A. & Li, W. Convergence: lactosylceramide-centric signaling pathways induce inflammation, oxidative stress, and other phenotypic outcomes. *Int. J. Mol. Sci.* **22**, 1816 (2021).

32 Bhunia, A. K., Han, H., Snowden, A. & Chatterjee, S. Lactosylceramide stimulates Ras-GTP loading, kinases (MEK, Raf), p44 mitogen-activated protein kinase, and c-fos expression in human aortic smooth muscle cells. *J. Biol. Chem.* **271**, 10660-10666 (1996).

33 Czarny, M., Liu, J., Oh, P. & Schnitzer, J. E. Transient mechanoactivation of neutral sphingomyelinase in caveolae to generate ceramide. *J. Biol. Chem.* **278**, 4424-4430 (2003).

34 Turner, D. G. P. *et al.* Neutral sphingomyelinase regulates mechanotransduction in human engineered cardiac tissues and mouse hearts. *J. Physiol.* **602**, 4387-4407 (2024).

35 Colom, A. *et al.* A fluorescent membrane tension probe. *Nat. Chem.* **10**, 1118-1125 (2018).

36 Nusshold, C. *et al.* Endocytosis and intracellular processing of BODIPY-sphingomyelin by murine CATH.a neurons. *Biochim. Biophys. Acta Mol. Cell Biol. Lipids* **1831**, 1665-1678 (2013).

37 Ginsburg, K. S. & Bers, D. M. Modulation of excitation-contraction coupling by isoproterenol in cardiomyocytes with controlled SR Ca^{2+} load and Ca^{2+} current trigger. *J. Physiol.* **556**, 463-480 (2004).

38 Bruning, J. C. *et al.* A muscle-specific insulin receptor knockout exhibits features of the metabolic syndrome of NIDDM without altering glucose tolerance. *Mol. Cell* **2**, 559-569 (1998).

39 Sohal, D. S. *et al.* Temporally regulated and tissue-specific gene manipulations in the adult and embryonic heart using a tamoxifen-inducible Cre protein. *Circ. Res.* **89**, 20-25 (2001).

40 Du, J. Y. *et al.* A small-molecule cocktail promotes mammalian cardiomyocyte proliferation and heart regeneration. *Cell Stem Cell* **29**, 545-558 (2022).

41 Ackers-Johnson, M. *et al.* A simplified, langendorff-free method for concomitant isolation of viable cardiac myocytes and nonmyocytes from the adult mouse heart. *Circ. Res.* **119**, 909-920 (2016).

42 Nakada, Y. *et al.* Hypoxia induces heart regeneration in adult mice. *Nature* **541**, 222-227 (2017).

43 Takagawa, J. *et al.* Myocardial infarct size measurement in the mouse chronic infarction model: comparison of area- and length-based approaches. *J. Appl. Physiol.* **102**, 2104-2111 (2007).

44 Lindsey, M. L., Kassiri, Z., Virag, J. A. I., Brás, L. E. D. & Scherrer-Crosbie, M. Guidelines for measuring cardiac physiology in mice. *Am. J. Physiol. Heart Circ. Physiol.* **314**, H733-H752 (2018).

45 Quaife-Ryan, G. A. *et al.* Multicellular transcriptional analysis of mammalian heart regeneration. *Circulation* **136**, 1123-1139 (2017).

46 Yurekten, O. *et al.* MetaboLights: open data repository for metabolomics. *Nucleic Acids Res.* **52**, D640-D646 (2023).

Fig. 1. KLF3 restrains the postnatal contractile programme to maintain CM homeostasis.

a, Relative Klf3 mRNA expression levels in mouse hearts collected at embryonic day 10 (E10), E13, E18, postnatal day 1 (P1), P7, and 2 months (2M), determined by quantitative RT–PCR. Data were first normalized to β-actin then to E10. n = 4 mice, except for E18, n = 3 mice. **b**, Representative immunoblot of KLF3 protein in mouse hearts at E13, E18, P1, P7 and 2M, with quantification normalized to GAPDH. n = 3 mice. **c**, Generation of CM-specific *Klf3* knockout (*Klf3*-cKO) mice. **d**, Immunoblot showing KLF3 protein expression in CMs isolated from 3-month-old Ctrl and *Klf3*-cKO mice. **e**, Quantification of KLF3 protein abundance shown in **d**, normalized to HSP90β. *n* = 3 mice. **f**, Representative hematoxylin and eosin (H&E) staining of heart sections from 3-month-old Ctrl and *Klf3*-cKO mice. *n* = 5 mice. Scale bar, 2 mm. **g-i**, Serial echocardiographic (ECHO) measurements of ejection fraction (**g**), fractional shortening (**h**) and heart rate (**i**) in 3-month-old Wt, Ctrl, and *Klf3*-cKO mice. *n* = 8 mice. **j**, Volcano plot showing differentially expressed genes in primary CMs isolated from 3-month-old Ctrl and *Klf3*-cKO mice. *n* = 4 mice. Selected contractile and Ca^{2+}-handling genes are highlighted. **k**,**l**, Gene Ontology (GO) enrichment analysis of upregulated (**k**) and downregulated (**l**) genes in adult CMs from Ctrl and *Klf3*-cKO mice. **m**,**n**, Representative sarcomere shortening traces (**m**) and quantification of sarcomere shortening, contraction velocity and relaxation velocity (**n**) of sarcomere shortening in CMs isolated from 3-month-old Ctrl and *Klf3*-cKO hearts. *n* = 4 mice; 26–33 CMs were analyzed per group for visualization. Statistical analysis was performed using mouse-

level averages. **o**,**p**, Representative Ca^{2+} transient traces (**o**) and quantification (**p**) in CMs isolated from 3-month-old Ctrl and *Klf3*-cKO hearts. **q**, Aggregation plots (top) and heatmaps (bottom) showing KLF3 CUT&Tag signal intensity centered on transcription start sites (TSSs; ±2 kb) across all protein-coding genes in CMs isolated from 3-month-old Ctrl and *Klf3*-cKO mice. Shown are average of $n = 3$ mice. **r**, Gene Ontology (GO) enrichment analysis of genes associated with differential KLF3 occupancy identified by CUT&Tag. Dot size represents gene number, and color indicates statistical significance ($-\log_{10}$ adjusted *P* value). **s**,**t**, Representative genome browser tracks showing KLF3 occupancy at the *Myh6* (**s**) and *Ryr2* (**t**) loci in CMs from 3-month-old Ctrl and *Klf3*-cKO heart, together with RNA-seq derived expression levels of the corresponding genes. Data points in **n** and **p** represent individual CMs; statistical analysis was performed using mouse-level averages. Data are mean ± s.e.m. One-way ANOVA followed by two-tailed Dunnett's multiple-comparison test were used for statistical analysis in **a**, **b**, **g**, **h** and **i**; Two-tailed, unpaired Student *t*-test was used for statistical analysis in **e**, **n**, **p**, **s** and **t**.

Fig. 2. *Klf3* loss reactivates CM proliferative competence.

a, Representative immunofluorescence (IF) images of Ki67 staining and quantification of $Ki67^+$ CMs in primary CMs isolated from P6 mouse hearts and transduced with adenoviruses expressing *cTnT-Klf3*-shRNA for 72 h. $n = 4$ mice. Scale bar, 20 μm. **b**, Representative IF images of Aurora B staining and quantification of Aurora B^+ CMs following infection with *cTnT-Klf3*-shRNA adenovirus. $n = 4$ mice. Scale bar, 20 μm.

913 **c**, Representative MADM images and quantification of the percentage of single-labeled
914 (red or green) CMs among total MADM-labeled CMs following infection with *cTnT-*
915 *Cre* adenovirus (MOI = 200), followed by transduction with AAV9 expressing cTnT-
916 *Klf3*-shRNA (MOI = 10^6). $n = 6$ mice. Scale bar, 100 μm. **d**,**e**, Representative IF images
917 of Ki67 staining and quantification of $Ki67^+$ CMs in heart sections from P24 (**d**) and
918 3M (**e**) Ctrl and *Klf3*-cKO mice. $n = 4$ mice. Scale bar, 20 μm. **f**, IF staining for WGA
919 and quantification of CM cross-sectional area in heart sections from 3-month-old Ctrl
920 and *Klf3*-cKO mice. $n = 4$ mice. Scale bar, 20 μm. **g**,**h**, Representative IF images of
921 sarcomeric α-actinin$^+$ CMs (**g**) isolated from 3-month-old Ctrl and *Klf3*-cKO mice, and
922 quantifications of CMs length and surface area (**h**). $n = 4$ mice, 30 adult CMs were
923 analyzed per mouse. Scale bar, 20 μm. **i**, Quantification of the proportions of mono-,
924 bi-, and multinucleated CMs. $n = 4$ mice, 30 adult CMs were analyzed per mouse. **j**,
925 Quantification of the total number of CMs per heart isolated from 3-month-old Ctrl and
926 *Klf3*-cKO hearts. $n = 4$ mice. **k**, IF staining for αSMA in heart sections from 3-month-
927 old Ctrl and *Klf3*-cKO mice. $n = 4$ mice. Scale bar, 20 μm. **l**, Western blot analysis of
928 Cyclin E1, $p21^{Waf1/Cip1}$ and Cyclin A2 protein expression in hearts from adult Ctrl and
929 *Klf3*-cKO mice. $n = 3$ mice. Data are presented as mean ± s.e.m. Two-tailed, unpaired
930 Student *t*-tests were used for statistical analysis.
931
932 **Fig. 3. *Klf3* suppression enhances post-infarction cardiac repair.**
933 **a**, Schematic illustrating the experimental timeline, including MI surgery (day 0) and
934 serial ECHO assessments at −1, 7, 30, and 67 days post-MI. **b**,**c**, Serial ECHO

measurements of left ventricular ejection fraction (**b**) and fractional shortening (**c**) in Ctrl and *Klf3*-cKO mice at indicated time points following MI. n = 10 mice. **d**, Representative Masson's trichrome staining of serial transverse heart sections from base to apex in Ctrl and *Klf3*-cKO mice at 67 days post-MI. Scale bar, 2 mm. **e**, Quantification of scar size expressed as the percentage of fibrotic midline length relative to total left ventricular midline length. **f**,**g**, Representative IF images and quantification of $Ki67^+$ (**f**) and $pH3^+$ (**g**) CMs in heart sections from Ctrl and *Klf3*-cKO mice at 67 days post-MI. n = 4 mice. Scale bar, 20 μm. **h**, Generation of TAM-inducible $Myh6^{MCM/+};Klf3^{fl/fl}$ (*Klf3*-iKO) mice. **i**, Representative H&E staining of heart sections from 3-month-old Ctrl-MCM and *Klf3*-iKO mice, 4 weeks post TAM withdrawal (wpTAM). n = 4 mice. Scale bar: 2 mm. **j**, Serial ECHO measurements of heart rate in Ctrl-MCM and *Klf3*-iKO mice at 4 wpTAM. n = 6 mice. **k**,**l**, Representative IF staining for WGA (**k**) and αSMA (**l**) in heart sections from 3-month-old Ctrl-MCM and *Klf3*-iKO mice at 4 wpTAM. n = 4 mice. Scale bar: 20 μm. **m**,**n**, Representative IF images and quantification for $pH3^+$ (**m**) and $Ki67^+$ (**n**) CMs in heart sections from 3-month-old Ctrl-MCM and *Klf3*-iKO mice at 4 wpTAM. n = 4 mice. Scale bar, 20 μm. **o**, Schematic illustrating the experimental timeline for MI surgery followed by TAM-induced *Klf3* deletion. **p**,**q** Serial ECHO measurements of left ventricular ejection fraction (**p**) and fractional shortening (**q**) in Ctrl-MCM and *Klf3*-iKO mice at the indicated time points following MI. n = 6 mice. **r**, Quantification of scar size in heart sections from Ctrl-MCM and *Klf3*-iKO mice at 8 wpMI. n = 6 mice. Scale bar, 2 mm. Data are presented as mean ± s.e.m. Two-tailed, unpaired Student t-tests were used for statistical analysis

957 in **e**, **f**, **g**, **j**, **k**, **l**, **m**, **n** and **r**; Two-way ANOVA followed by two-tailed Dunnett's
958 multiple-comparison test was used for statistical analysis of panels **b** and **c**;
959 Longitudinal measurements in **p** and **q** were analyzed using a linear mixed-effects
960 model, followed by Sidak's multiple-comparison test for between-group comparisons
961 at individual time points.
962
963 **Fig. 4. *Klf3* loss promotes a LacCer enriched glycosphingolipid programme.**
964 **a-d**, Untargeted metabolomics profiling in positive and negative ion mode were
965 performed on primary CMs isolated from 3-month-old Ctrl and *Klf3*-cKO mice. $n = 4$
966 mice. **a**,**b** Volcano plot in positive (**a**) and negative (**b**) ion mode showing differentially
967 abundant metabolites between groups, plotted as $\log_2$(FC) versus $-\log_{10}$(*P* value). **c**,**d**
968 Metabolic pathway impact analysis highlighting significantly altered pathways in
969 positive (**c**) and negative (**d**) ion mode. **e**, Overlap analysis of enriched pathways
970 identified by transcriptomic and metabolomic profiling in *Klf3*-cKO CMs. **f**, Relative
971 abundance of LacCer (d18:1/16:0) and LacCer (d18:1/20:0) determined by targeted
972 lipidomic analysis in CMs isolated from 3-month-old Ctrl and *Klf3*-cKO mice. $n = 4$
973 mice. **g**, Representative CUT&Tag genome browser tracks showing KLF3 occupancy
974 at the *B4galt6* locus in 3-month-old Ctrl and *Klf3*-cKO CMs. **h**,**i** Representative
975 immunoblot (**h**) and quantification (**i**) of B4GALT6 protein levels in adult Ctrl and
976 *Klf3*-cKO CMs. $n = 3$ mice. **j**, IF staining for LacCer (Huly-m13) and WGA in heart
977 sections from 3-month old Ctrl and *Klf3*-cKO mice. $n = 4$ mice. Scale bar: 20 μm. **k**,
978 Representative IF images of Aurora B staining and quantification of Aurora B^+ CMs

following treatment of primary rat CMs with increasing concentrations of LacCer (d18:1/16:0). Scale bar, 20 μm. **l**, Representative IF images of Ki67 staining and quantification of $Ki67^+$ CMs following treatment with 0.5 μM LacCer. Scale bar, 50 μm. n = 5 rats. Primary CMs were independently isolated from each rat. Data are presented as mean ± s.e.m. Two-tailed, unpaired Student t-tests were used for statistical analysis in **f**, **i** and **l**; One-way ANOVA followed by two-tailed Dunnett's multiple-comparison test was used for statistical analysis in **k**.

Fig. 5. Contractile stress activates nSMase-dependent sphingolipid signaling.

a, Quantification of Cer abundance determined by targeted lipidomic analysis in Ctrl and *Klf3*-cKO CMs isolated from 3-month-old heart. n = 4 mice. **b**, Representative FLIM images of Flipper-TR-labelled CMs isolated from P6 Wt and $Klf3^{fl/fl}$ mice following transduction with *cTnT-Cre* adenovirus. Flipper-TR lifetime (τ) was quantified as a measure of membrane-associated mechanical stress. n = 4 mice. Primary CMs were independently isolated from each mouse. **c**, Representative images of BODIPY-SM fluorescence in primary CMs isolated from P6 Wt and $Klf3^{fl/fl}$ mice following transduction with *cTnT-Cre* adenovirus and AAV9 expressing *cTnT-infrared fluorescent protein (IFP)* for 7 days. CMs were subsequently treated with the nSMase inhibitor GW4869 or cultured in low-Ca^{2+} medium (0.1 mM). n = 4 mice. Primary CMs were independently isolated from each mouse. Scale bar, 20 μm. **d**, Quantification of Cer abundance determined by targeted lipidomic analysis in Ctrl and *Klf3*-deficient CMs following 72 h treatment with physiological Ca^{2+} (1.8 mM), low Ca^{2+} (0.1 mM),

or GW4869 (2 μM). n = 4 mice. Primary CMs were independently isolated from each mouse. **e**,**f**, Quantification of the percentages of Aurora B^+ (**e**) and $Ki67^+$ (**f**) CMs following the same treatments. n = 5 mice, Primary CMs were independently isolated from each mouse. **g**, Representative FLIM images and quantification of Flipper-TR FLIM in primary rat CMs treated with DMSO or isoproterenol (ISO, 2 μM). n = 4 rats. Primary CMs were independently isolated from each rat. **h**, Representative images of BODIPY-SM fluorescence in rat CMs treated with DMSO (Ctrl), ISO (2 μM), or ISO plus GW4869 (20 μM). n = 4 rats. Primary CMs were independently isolated from each rat. Scale bars, 20 μm. **i**,**j**, Representative IF images and quantification of Aurora B^+ (**i**) and $Ki67^+$ (**j**) CMs following treatment with DMSO, ISO, or ISO plus GW4869. n = 5 rats. Primary CMs were independently isolated from each rat. Scale bars, 20 μm. Data are presented as mean ± s.e.m. Two-tailed, unpaired Student t-tests were used for statistical analysis in **a**, **b** and **g**; One-way ANOVA followed by two-tailed Dunnett's multiple-comparison test was used for statistical analysis in **d**, **e**, **f**, **i** and **j**.

Fig. 6. LacCer enhances post-infarction cardiac repair.

a, Schematic illustrating the experimental timeline for MI surgery and LacCer administration. **b**, Representative M-mode ECHO images from Ctrl and LacCer-treated mice at 9 wpMI. Yellow lines indicate left ventricular dimensions used for functional measurements. **c**–**f**, Serial ECHO analysis of left ventricular ejection fraction (**c**), fractional shortening (**d**), left ventricular end-diastolic volume (LV Vol;d, **e**) and end-systolic volume (LV Vol;s, **f**) in Vehicle (n = 11 mice) and LacCer (n = 10 mice) treated

mice at the indicated time points after MI. **g**,**h**, Representative Masson's trichrome staining (**g**) and quantification of scar size (**h**) in heart sections from Ctrl and LacCer-treated mice at 9 weeks post MI. $n = 9$ mice. Scale bar, 2 mm. Data are presented as mean ± s.e.m. For statistical analysis, longitudinal measurements in **c**–**f** were analyzed using a linear mixed-effects model, followed by Sidak's multiple-comparison test for between-group comparisons at individual time points; two-tailed unpaired Student *t*-tests were used in **h**.

1030 **Figure 1**

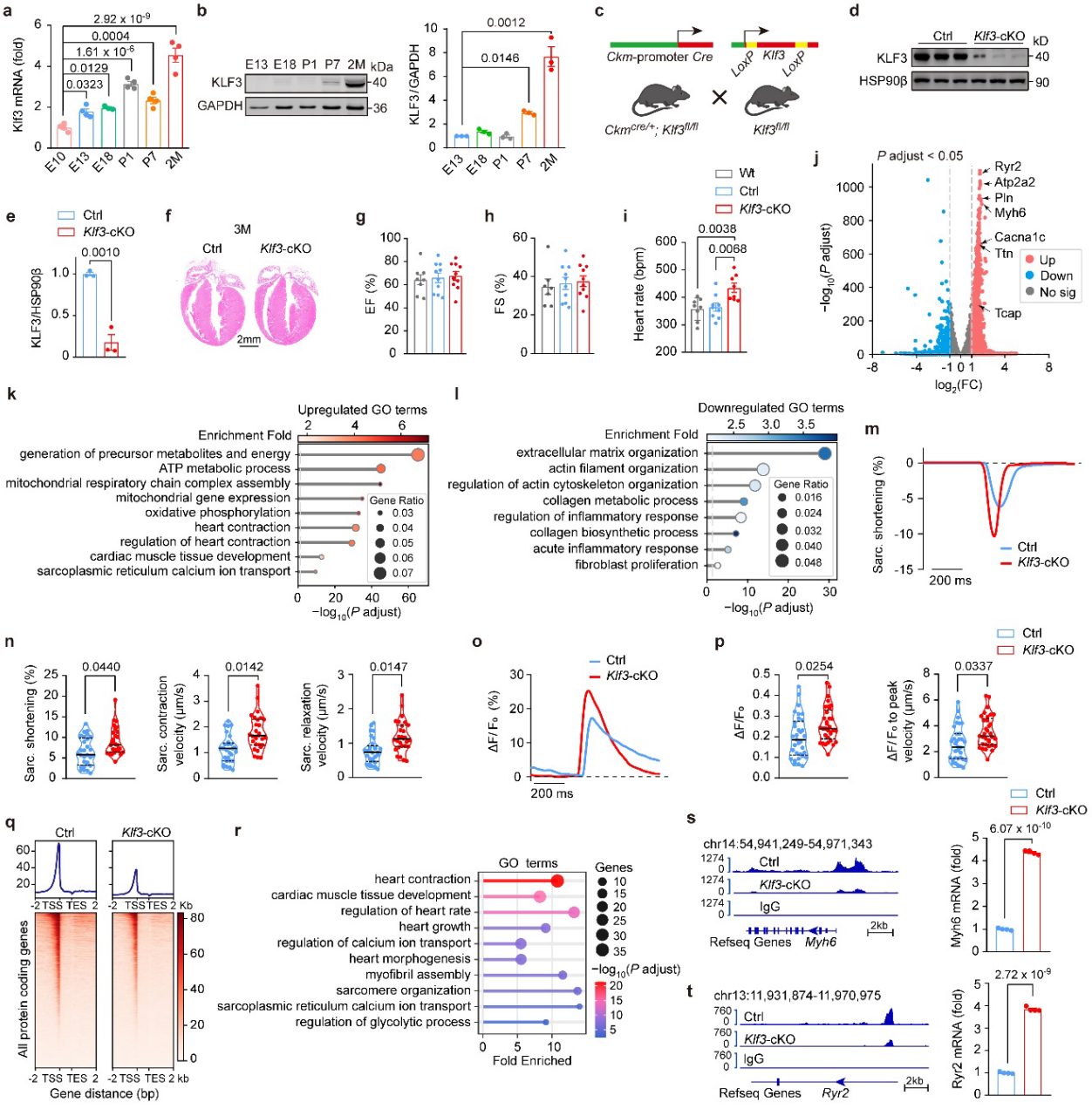

1031

1032

Figure 2

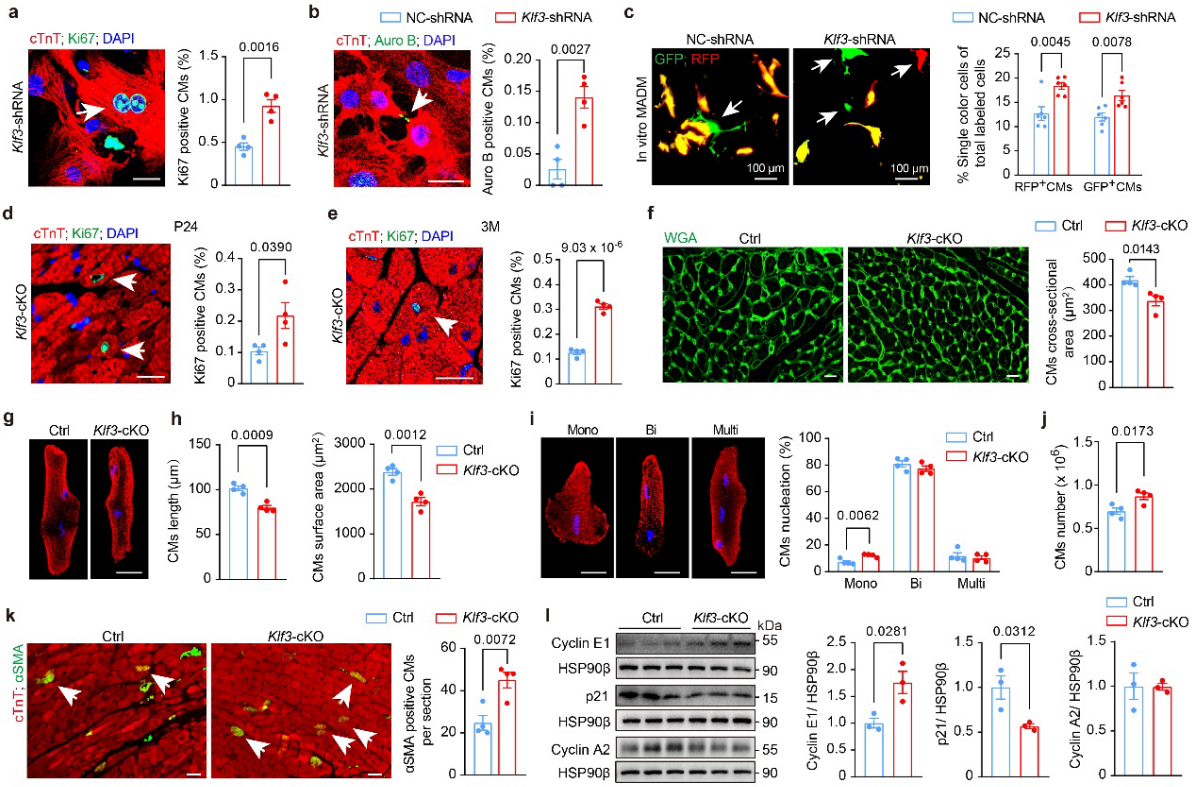

Figure 3

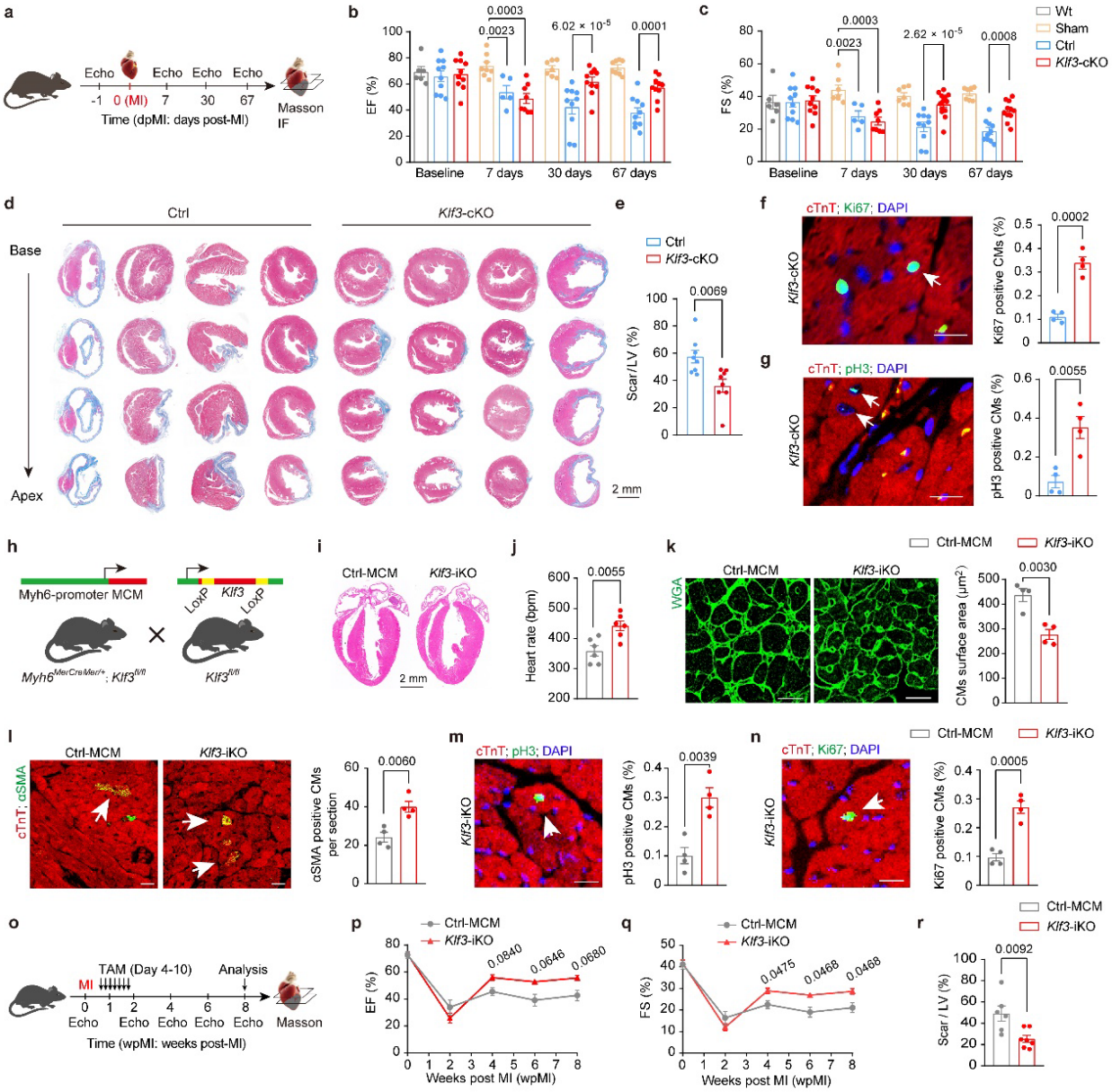

1039 **Figure 4**

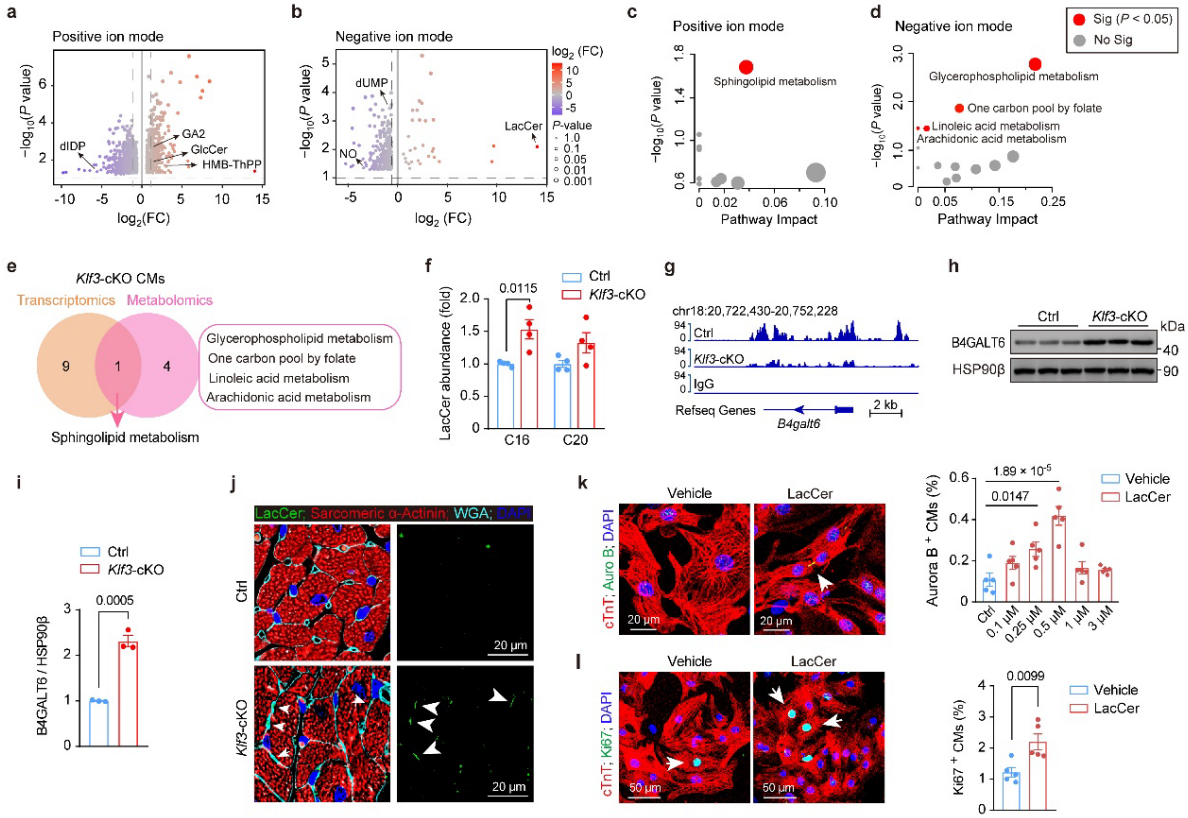

1040

1041 **Figure 5**

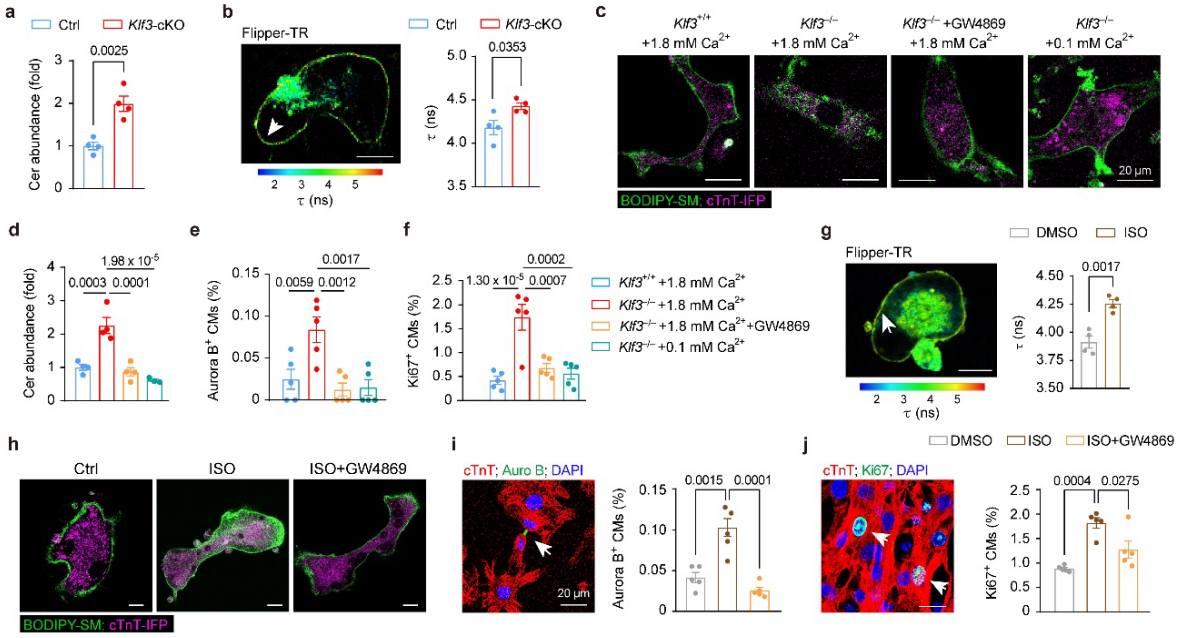

1042

1043 **Figure 6**

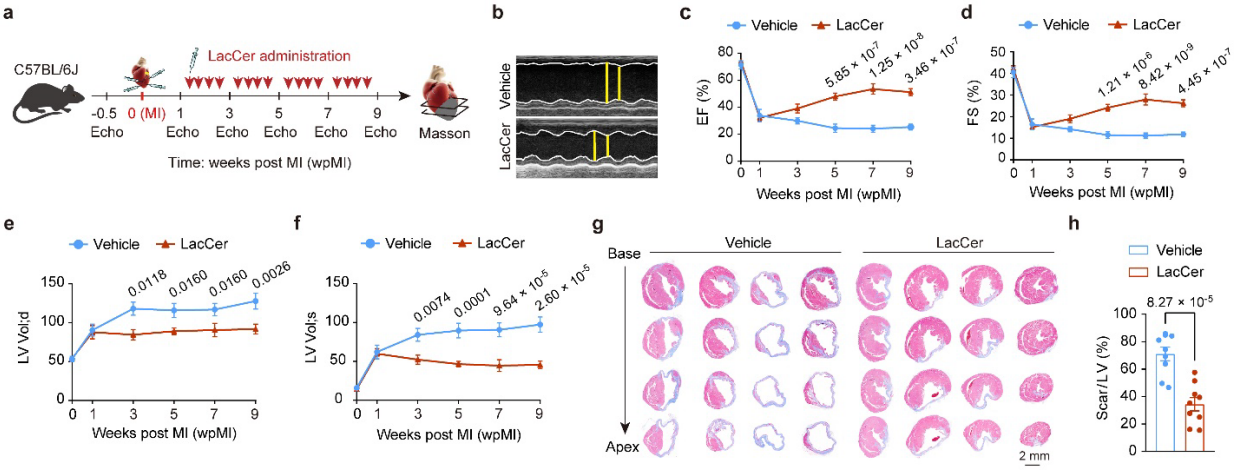

1044

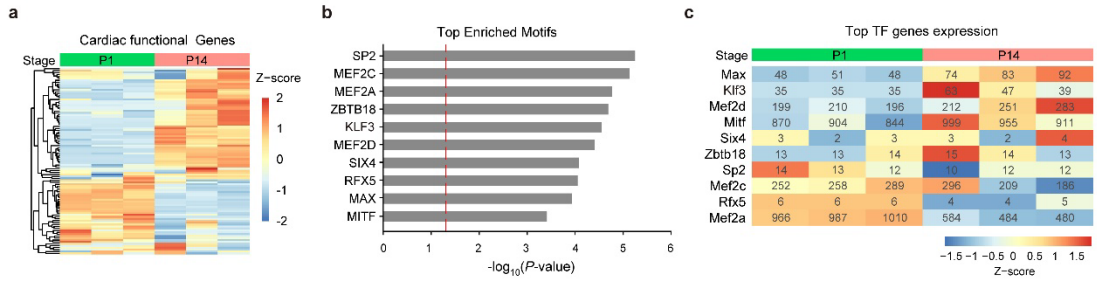

Extended Data Fig. 1. KLF3 as a candidate regulator of the maturation-associated contractile genes.

a, Heatmap showing the expression of representative cardiac functional genes in CMs derived from P1 and P14 mice. Gene expression values for genes involved in cardiac contraction and Ca^{2+} handling were normalized by Z-score and hierarchically clustered. **b,** Top 10 transcription factor-binding motifs enriched in regulatory regions (±2 kb around TSS) associated with genes upregulated in P14 CMs, identified by HOMER motif analysis. Motifs are ranked according to significance ($-\log_{10}(P$ value)). The dashed red line indicates the significance threshold (P = 0.05). **c**, Heatmap showing the expression levels of the top 10-enriched-transcription factors in CMs derived from P1 and P14 mice. Gene expression values were normalized by Z-score. Numbers in the middle of each square show TPM value of each gene in P1 and P14 CMs.

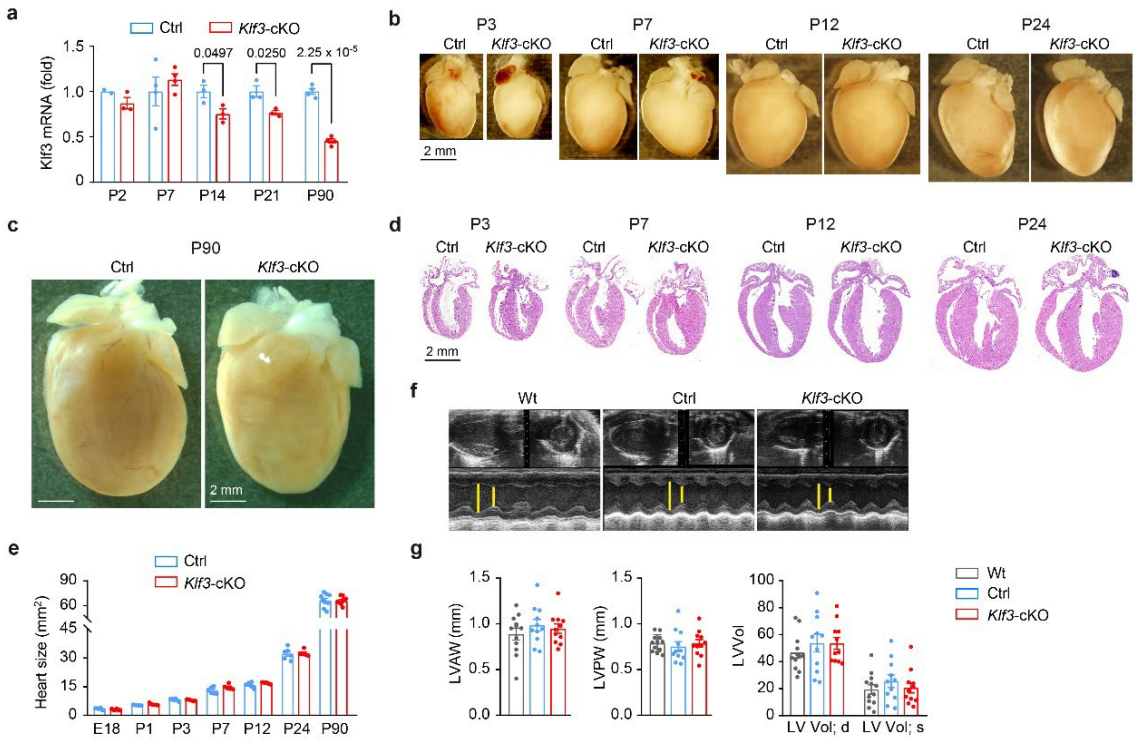

Extended Data Fig. 2. *Klf3* deficiency does not affect heart morphogenesis and function.

a. RNA-seq analysis showing expression levels of targeted exon (Exon 3) of *Klf3* in primary CMs isolated at different stages of heart maturation. Primary CMs were independently isolated from independent mice. P2 Ctrl, n = 2 mice. For P7, P14, P21 and P90, n = 3−4 mice. **b-d**, Representative gross morphology (**b**,**c**) and H&E staining (**d**) of hearts at different stages of heart maturation. Scale bar, 2 mm. **e**, Quantification of heart size at different stages of heart maturation. *n* = 5−10 mice. **f**, Representative B-mode and M-mode ECHO images from 3-month-old Ctrl and *Klf3*-cKO mice. Yellow lines indicate left ventricular dimensions used for functional measurements. **g**, Serial ECHO analysis of left ventricular anterior wall thickness (LVAW), left ventricular posterior wall thickness (LVPW), end-diastolic volume (LV Vol;d) and end-systolic volume (LV Vol;s) in 3-month-old Ctrl and *Klf3*-cKO mice. *n* = 11 mice. Data are presented as mean ± s.e.m. Two-tailed, unpaired Student *t*-tests were used for statistical analysis in **a** and **e**; One-way ANOVA followed by two-tailed Dunnett's multiple-comparison test were used for statistical analysis in **g**.

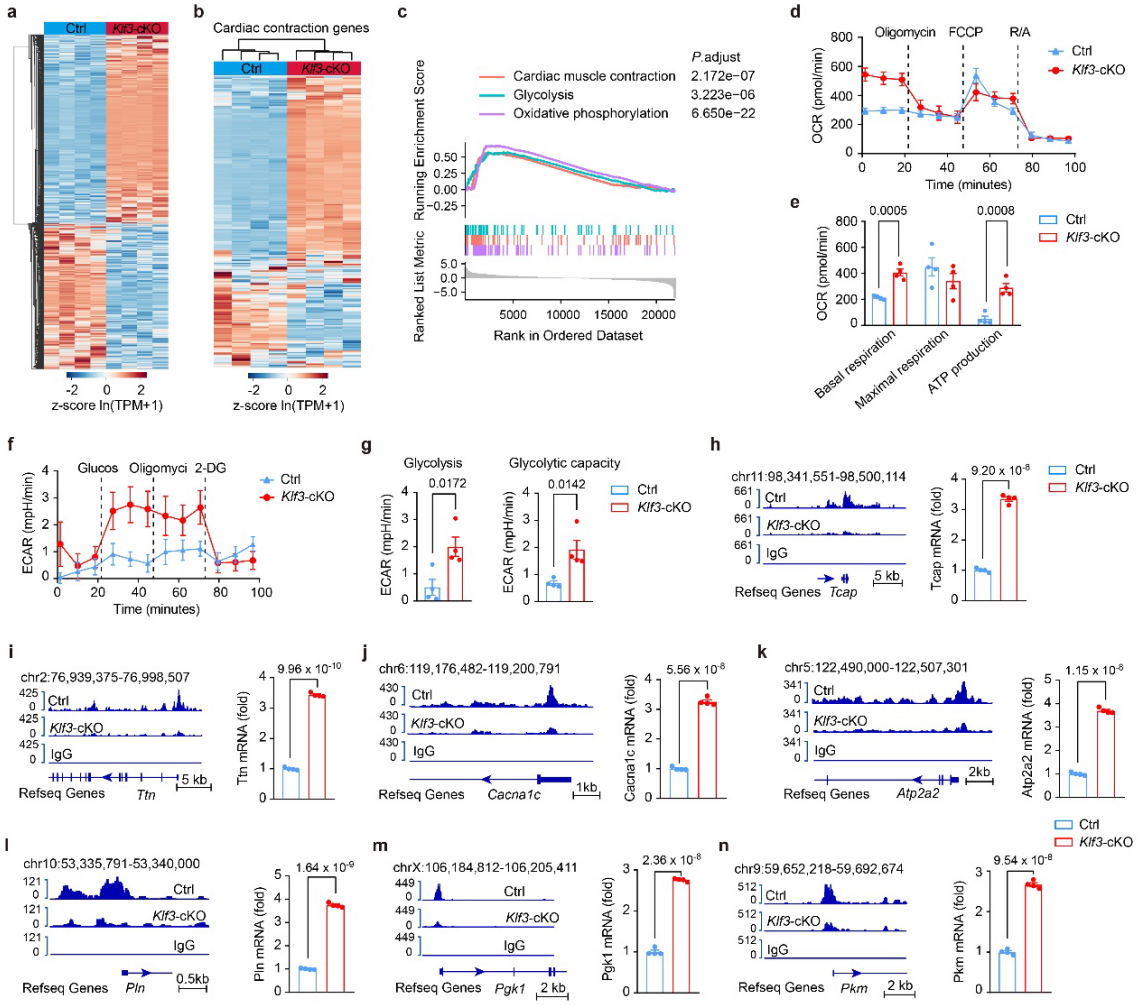

Extended Data Fig. 3. KLF3 restrains cardiac contractile programmes and respiratory remodeling.

a, Heatmap showing differentially expressed genes between 3-month-old Ctrl and *Klf3*-cKO CMs identified by RNA-sequencing. Gene expression values were normalized by Z-score of $\log_2$(TPM+1). $n = 4$ mice. **b,** Heatmap showing the expression profiles of genes associated with cardiac contraction in Ctrl and *Klf3*-cKO CMs. **c,** Gene set enrichment analysis (GSEA) showing enrichment of pathways related to cardiac muscle contraction, glycolysis, and oxidative phosphorylation in *Klf3*-cKO CMs compared with Ctrl. Adjusted *P* values are indicated. **d,** Oxygen consumption rate (OCR) measured by Seahorse extracellular flux analysis in 3-month-old Ctrl and *Klf3*-cKO CMs following sequential treatment with oligomycin, FCCP, and rotenone/antimycin A (R/A). **e,** Quantification of basal respiration, maximal respiration,

and ATP production derived from OCR measurements shown in **d.** $n = 4$ mice. Primary CMs were independently isolated from each mouse. **f,** Extracellular acidification rate (ECAR) measured by Seahorse glycolytic stress assay in 3-month-old Ctrl and *Klf3*-cKO CMs following sequential addition of glucose, oligomycin, and 2-deoxyglucose (2-DG). **g,** Quantification of glycolysis and glycolytic capacity derived from ECAR measurements shown in **f**. $n = 4$ mice. Primary CMs were independently isolated from each mouse. **h**-**n**, Representative CUT&Tag genome browser tracks showing KLF3 occupancy at the *Tcap* (**h**), *Ttn* (**i**), *Cacna1c* (**j**), *Atp2a2* (**k**), *Pln* (**l**), *Pgk1* (**m**) and *Pkm* (**n**) loci in Ctrl and *Klf3*-cKO CMs, along with quantification of corresponding gene expression levels. $n = 4$ mice. Primary CMs were independently isolated from each 3-month-old mouse. Data are presented as mean ± s.e.m. Statistical significance were determined using two-tailed unpaired Student's *t*-tests in **e**, **g**-**n**.

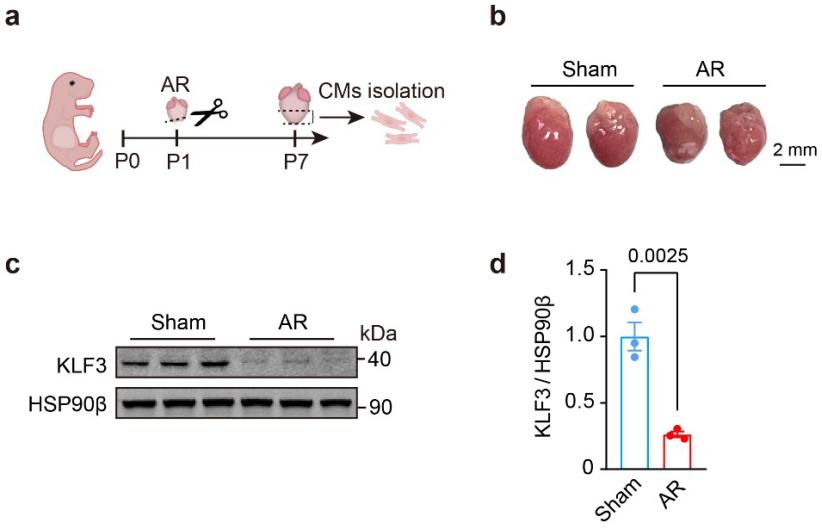

Extended Data Fig. 4. KLF3 is suppressed following neonatal apical resection.

a, Experimental schematic illustrating neonatal apical resection (AR) performed at P1 and isolation of CMs at P7 for subsequent analyses. **b**, Representative gross morphology of hearts collected from sham-operated and AR mice at P7. Scale bar, 2 mm. **c**, Representative immunoblot showing KLF3 protein expression in CMs isolated from the regenerative zone at P7 following AR. $n = 3$ mice. HSP90β served as a loading control. **d**, Quantification of KLF3 protein abundance shown in **c**, normalized to HSP90β. Data are presented as mean ± s.e.m. Statistical significance was determined using two-tailed unpaired Student's *t*-tests in **d**.

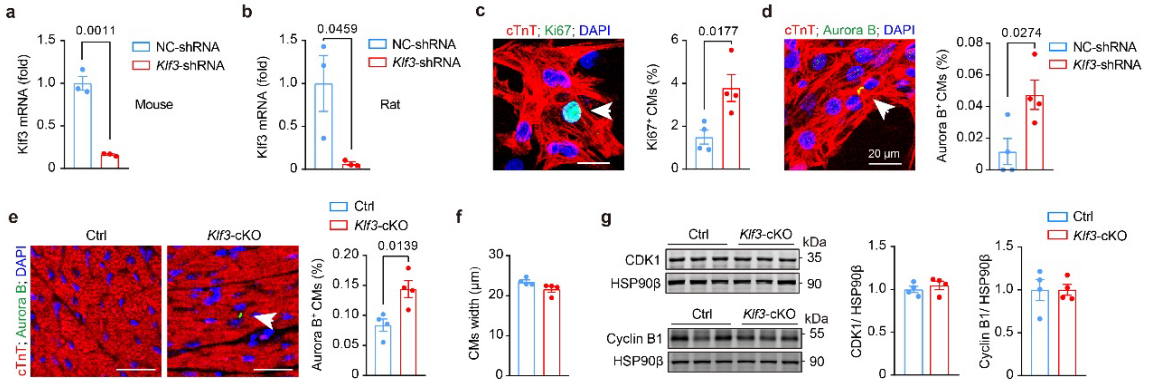

Extended Data Fig. 5. *Klf3* deficiency induces CM proliferation.

a, Knockdown efficiency of *Klf3*-shRNA adenovirus in mouse CMs. $n = 3$ mice. Primary CMs were independently isolated from each mouse. **b**, Knockdown efficiency of *Klf3*-shRNAs adenovirus in rat CMs. $n = 3$ rats. Primary CMs were independently isolated from each rat. **c**, Representative IF images of Ki67 staining and quantification of Ki67$^+$ CMs following infection with *cTnT-Klf3*-shRNA adenovirus. $n = 4$ rats. Primary CMs were independently isolated from each rat. Scale bar, 20 μm. **d**, Representative IF images of Aurora B staining and quantification of Aurora B$^+$ CMs following infection with *cTnT-Klf3*-shRNA adenovirus. $n = 4$ rats. Primary CMs were independently isolated from each rat. Scale bar, 50 μm. **e**, Representative IF images of Aurora B staining and quantification of Aurora B$^+$ CMs in heart sections from P24 Ctrl and *Klf3*-cKO mice. $n = 4$ mice. Scale bar: 20 μm. **f**, Quantifications of CMs width in 3-month-old Ctrl and *Klf3*-cKO mice. $n = 3$ mice, 30 adult CMs were analyzed per mouse. **g**, Western blot analysis of CDK1 and Cyclin B1 protein expression in adult Ctrl and *Klf3*-cKO heart. $n = 3$ mice. Data are presented as mean ± s.e.m. Statistical significance was determined using two-tailed unpaired Student's *t*-tests.

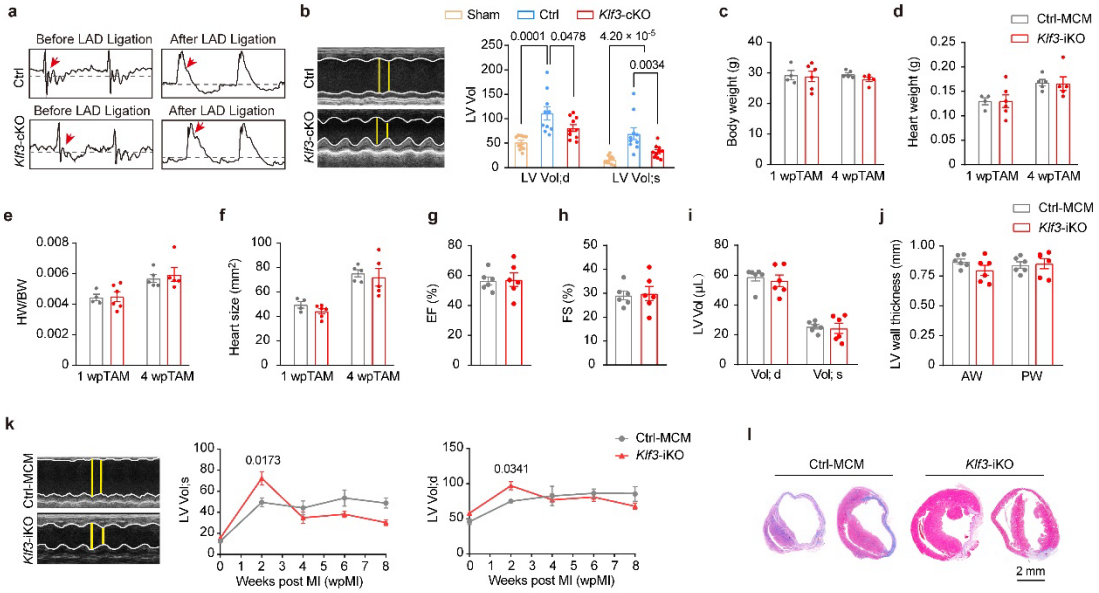

Extended Data Fig. 6. Inducible *Klf3* knockout does not affect heart function.

a. Representative electrocardiogram (ECG) traces from Ctrl and *Klf3*-cKO mice before and after LAD coronary artery ligation. ST-segment elevation (red arrows) after ligation indicates successful MI surgery. **b**, Representative M-mode ECHO images and quantification of left ventricular end-diastolic volume (LV Vol;d) and end-systolic volume (LV Vol;s) at 67 days post-MI (or Sham) in Ctrl and *Klf3*-cKO mice. $n = 10$ mice. **c-f**, Body weight (**c**), heart weight (**d**), heart weight-to-body weight ratio (HW/BW) (**e**), and quantification of heart size (**f**) in 3-month-old Ctrl-MCM and *Klf3*-iKO mice at 1 and 4 wpTAM. $n = 4–6$ mice. **g-j**, Serial ECHO assessment of left ventricular ejection fraction (**g**), fractional shortening (**h**), end-diastolic and end-systolic volume (**i**), and left ventricular anterior and posterior wall thickness (**j**) in 3-month-old Ctrl-MCM and *Klf3*-iKO mice at 4 wpTAM. $n = 6$ mice. **k**, Representative M-mode ECHO images from Ctrl-MCM and *Klf3*-iKO mice at 8 wpMI, and Serial ECHO analysis of left ventricular fractional shortening, end-systolic volume and end-diastolic volume in Ctrl-MCM and *Klf3*-iKO mice at indicated time points after MI. $n = 6$ mice. **l**, Representative Masson's trichrome staining in heart sections from Ctrl-MCM and *Klf3*-iKO mice at 8 wpMI. $n = 6$ mice. Scale bar, 2 mm. Data are presented as mean ± s.e.m. One-way ANOVA followed by two-tailed Dunnett's multiple-comparison test was used for statistical analysis in **b**. Two-

tailed, unpaired Student *t*-tests were used for statistical analysis in **c**–**j**; Longitudinal measurements in **k** were analyzed using a linear mixed-effects model with Sidak's multiple-comparison test for pairwise comparisons at individual time points.

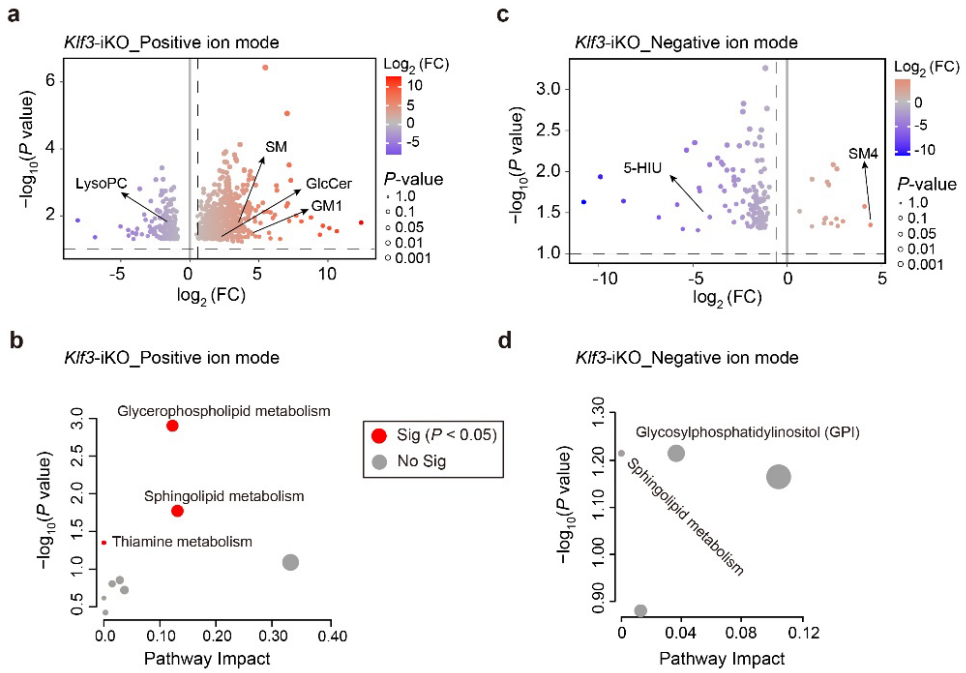

Extended Data Fig. 7. *Klf3* knockout rewires CM metabolism.

a,**b**, Untargeted metabolomics of primary CMs from 3-month-old Ctrl-MCM (n = 4 mice) and *Klf3*-iKO mice (n = 3 mice) at 1 wpTAM, analyzed in positive ion mode. **a**, Volcano plot of differential metabolites. **b**, Pathway enrichment analysis of differential metabolites. **c**,**d**, Untargeted metabolomics of primary CMs from Ctrl-MCM and *Klf3*-iKO mice analyzed in negative ion mode. **c**, Volcano plot of differential metabolites. **d**, Pathway enrichment analysis of differential metabolites.

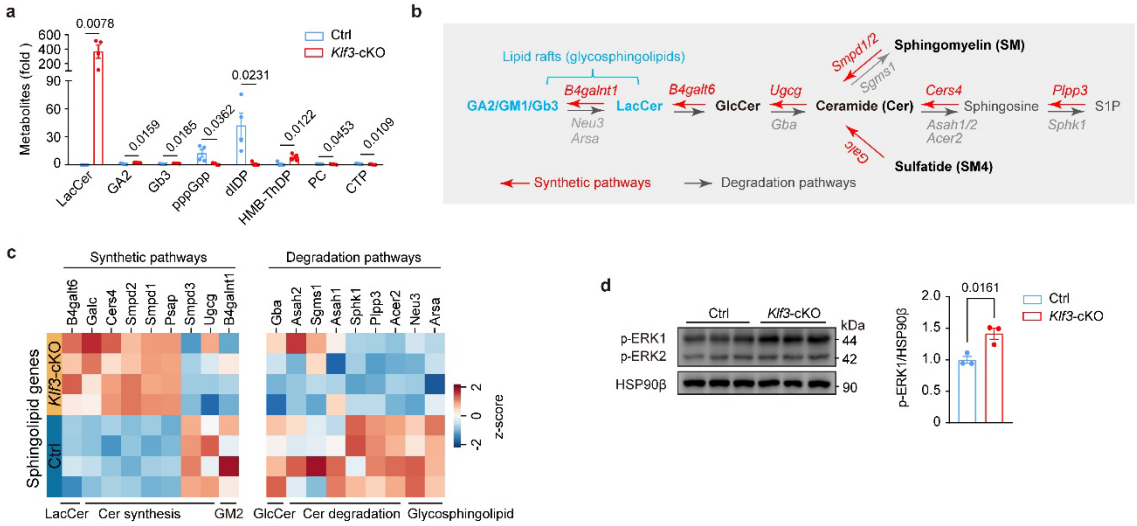

Extended Data Fig. 8. KLF3 deficiency drives sphingolipid biosynthetic metabolism.

a, Relative abundance of significantly changed metabolites within the 5 pathways commonly enriched by transcriptomic and untargeted metabolomic analyses in adult Ctrl and *Klf3*-cKO CMs. **b**, Schematic overview of sphingolipid metabolic pathways. Sphingolipid species altered in *Klf3*-iKO CMs at 1 wpTAM are highlighted in black and are predominantly associated with intermediate metabolites in the biosynthetic pathway. In contrast, metabolites accumulated in CMs from *Klf3*-cKO hearts and *Klf3*-iKO hearts at 4 wpTAM are highlighted in blue and are mainly enriched at the distal end of the glycosphingolipid biosynthetic pathway. Red arrows indicate biosynthetic reactions, whereas gray arrows denote degradation pathways. **c**, Heatmap showing expression profiles of sphingolipid metabolism-related genes identified by RNA sequencing in adult Ctrl and *Klf3*-cKO CMs. Gene expression values were normalized by Z-score. **d**, Representative immunoblot and quantification of phosphorylated ERK1/2 (p-ERK1/2) levels in adult Ctrl and *Klf3*-cKO hearts. n = 3 mice. Data are presented as mean ± s.e.m. Statistical significance was determined by unpaired two-tailed Student's *t*-tests in **a** and **d**.

Supplementary Information

Supplementary Table 1: Primer sequences used in this study.

Supplementary Table 2: Animal numbers included_excluded and lost during in vivo experiments.

Supplementary Table 3: Cardiac maturation-related genes.

Supplementary Table 4: shRNA sequences used in this study.